HAL open science

Rancho Seco monogenetic volcano (Michoacán, Mexico): Petrogenesis and lava flow emplacement based on LiDAR images

Israel Ramírez-Uribe, Claus Siebe, Magdalena Oryaëlle Chevrel, Christopher Fisher

▶ **To cite this version:**

Israel Ramírez-Uribe, Claus Siebe, Magdalena Oryaëlle Chevrel, Christopher Fisher. Rancho Seco monogenetic volcano (Michoacán, Mexico): Petrogenesis and lava flow emplacement based on LiDAR images. Journal of Volcanology and Geothermal Research, 2021, 411, pp.107169. 10.1016/j.jvolgeores.2020.107169 . hal-03113443v1

HAL Id: hal-03113443

https://uca.hal.science/hal-03113443v1

Submitted on 14 Nov 2022 (v1), last revised 7 Mar 2023 (v2)

HAL is a multi-disciplinary open access archive for the deposit and dissemination of scientific research documents, whether they are published or not. The documents may come from teaching and research institutions in France or abroad, or from public or private research centers.

L'archive ouverte pluridisciplinaire **HAL**, est destinée au dépôt et à la diffusion de documents scientifiques de niveau recherche, publiés ou non, émanant des établissements d'enseignement et de recherche français ou étrangers, des laboratoires publics ou privés.

Distributed under a Creative Commons Attribution - NonCommercial - NoDerivatives 4.0 International License

Rancho Seco monogenetic volcano (Michoacán, Mexico): Petrogenesis and lava flow emplacement based on LiDAR images

Israel Ramírez-Uribe [a,*], Claus Siebe [a], Magdalena Oryaëlle Chevrel [b], Christopher T. Fisher [c]

[a] Departamento de Vulcanología, Instituto de Geofísica, Universidad Nacional Autónoma de México, Coyoacán, C.P. 04510 Ciudad de México, Mexico
[b] Université Clermont Auvergne, CNRS, IRD, OPGC, Laboratoire Magmas et Volcans, F-63000 Clermont-Ferrand, France
[c] Department of Anthropology, Colorado State University, Fort Collins CO-80523, USA

Keywords:
Michoacán-Guanajuato Volcanic Field
Monogenetic volcanism
Andesite lava flows
Rheology
LiDAR
Eruption dynamics

A B S T R A C T

Given the high eruption recurrence in the Michoacán-Guanajuato volcanic field (MGVF) in central Mexico, the birth of a new monogenetic volcano can be expected in the future. It is important, therefore, to reconstruct the past eruptions of its many different volcanoes, including estimates of lava flow emplacement times and their rheological properties. These studies define the range of possible future eruptive scenarios and are necessary to evaluate potential risk. The Rancho Seco monogenetic volcano, located in the central part of the MGVF (19°37′03"N, 101°28′21"W), was radiocarbon-dated at ~27,845 years BP. Its eruption initiated with a violent-Strombolian phase that produced a scoria cone and was followed by the effusion of at least seven associated andesitic lava flows, reflecting drastic changes in the eruptive dynamics. Effusive activity probably involved decreases in the magma ascent and discharge rates linked to efficient degassing in an open system. Lava chemical composition suggest an origin of partial melting of a subduction-modified hydrated heterogenous mantle wedge and textural and mineralogical analysis indicates significant crystal fractionation and minor assimilation of granodioritic basement rocks. High-resolution LiDAR imagery was used to estimate lava flow viscosities and emplacement times by following a morphology-based methodology. Results indicate that lava flow viscosities ranged from 10^5 to 10^9 Pa·s and emplacement durations between 32 and 465 days for the flow units considered (F5 and F6). The entire eruption may have lasted from 2 to 6 years with a mean effusion rate of 4 to 15 m^3/s. Our results are also pertinent to archaeologists studying the architectural remains of Angamuco, a large urban pre-Hispanic site built on Rancho Seco's lava flows.

1. Introduction

The Trans-Mexican Volcanic Belt (TMVB) is a continental volcanic arc containing ~8000 volcanic structures (Demant, 1978; Gómez-Tuena et al., 2005), and is tectonically related to the subduction of the oceanic Cocos and Rivera plates underneath the North American continental plate along the Mesoamerican trench (Nixon, 1982; Pardo and Suárez, 1995; Gómez-Tuena et al., 2005). It is important to highlight that since pre-Hispanic times this geologic province has grown in population and economic activity (Siebe and Macías, 2006; Ferrari et al., 2012). In the states of Guanajuato and Michoacán, the TMVB overlaps the older Oligocene to middle Miocene Sierra Madre Occidental (SMO) volcanic arc and a complex prevolcanic basement (Pasquaré et al., 1991).

The Michoacán-Guanajuato Volcanic Field (MGVF) is situated in the central part of the TMVB (Fig. 1) and comprises more than 1400 Quaternary monogenetic eruptive centres (including Rancho Seco volcano) distributed over an area of 40,000 km^2 (Hasenaka and Carmichael, 1985). It has one of the greatest concentrations of monogenetic volcanoes within a subduction zone in the world (Hasenaka and Carmichael, 1985; Hasenaka, 1994). It is bounded to the north by the valley of the Lerma river and to the south by the depression of the Balsas river (Fig. 1); to the east it is contained by the Tzitzio anticline (Blatter and Hammersley, 2010), and to the west by the so-called "Mazamitla Volcanic Gap" (Kshirsagar et al., 2015). The MGVF contains mainly scoria cones and associated lavas, but also isolated thick lava flows, domes, maars, and tuff rings. In addition, there are approximately 400 volcanic edifices described as small or medium-sized shield volcanoes (Hasenaka and Carmichael, 1985; Hasenaka, 1994; Chevrel et al., 2016a) and only two stratovolcanoes (Tancítaro and Patamban), both considered extinct (Ownby et al., 2007; Siebe et al., 2014). Two historical eruptions have been witnessed in this field, Jorullo (1759–1774) and Paricutin (1943–1952), hinting that the future birth of a new volcano is highly likely (e.g. Guilbaud et al., 2011; Luhr and Simkin, 1993). Recent studies of areas within the MGVF (e.g. Guilbaud et al., 2011, 2012, 2019; Siebe et al., 2014; Kshirsagar et al., 2015, 2016; Chevrel et al., 2016a, 2016b; Larrea et al., 2017, 2019; Reyes-Guzmán et al., 2018;

* Corresponding author.
E-mail address: isramirez.u@gmail.com (I. Ramírez-Uribe).

Fig. 1. Satellite image (Microsoft® Bing Maps, 2019) of the Michoacán–Guanajuato Volcanic Field (MGVF, outlined in red) showing the location of the Rancho Seco (RS) volcano study area (yellow rectangle denotes area covered in Fig. 3). Red triangles indicate volcanoes mentioned in the text. Major fault systems are CFS=Cuitzeo Fault System, CTFS=Chapala–Tula Fault System, COFS=Chapala–Oaxaca Fault System, and QFTS=Querétaro–Taxco Fault System. Inset map at lower right corner shows location of the MGVF (study area) within the TMVB and major plate-tectonic features. (For interpretation of the references to colour in this figure legend, the reader is referred to the web version of this article).

Osorio-Ocampo et al., 2018; Pérez-Orozco et al., 2018; Ramírez-Uribe et al., 2019) have shown that eruptions have not only been diverse in style, but also frequent during Late Pleistocene and Holocene time.

The Rancho Seco monogenetic volcano is an andesitic scoria cone associated with lava flows situated at the eastern margin of the Pátzcuaro lake basin (Fig. 1) in the state of Michoacán and dated at 27,845 +445/−425 years BP (before present) (Ramírez-Uribe et al., 2019). The availability of LiDAR imagery provides the means to precisely map the lava flows, determine their volumes, highlight their main morphological features in great detail and measure their geometric parameters. We, then, apply morphology-based methods to estimate flow emplacement duration and effusion rates. In addition, chemical and petrological analyses of distinct lava units were used to constrain the magma source, storage conditions, and lava rheology, and to propose an eruptive model. These parameters are crucial for constraining future eruptive scenarios and evaluating potential volcanic risk.

2. Background

Lava flow hazards depend on several factors, namely the rheology of the lava and its effusion rate, the topography of the existing terrain, and the distance reached by the flow front before it entirely solidifies. The interpretation of remote observations of ancient flows can be helpful in understanding their emplacement dynamics. Flow geometry, structure, and surface morphology offer hints about eruption rates and lava rheology (Hulme, 1974; Griffiths, 2000). The evolution of a lava flow depends on many factors including effusion rate, underlying topography, and the rheology of the lava, which changes during degassing and cooling (Castruccio et al., 2013). Rheological models have been developed to estimate the apparent viscosity of lava flows based on their dimensions (e.g., Nichols, 1939; Hulme, 1974; Griffiths and Fink, 1993; Pinkerton and Wilson, 1994; Kerr and Lyman, 2007; Castruccio et al., 2013). Currently, instruments to directly measure active lava flow viscosities greater than 10^5 Pa·s (typical for evolved compositions such as andesites, dacites, and rhyolites) are not available and viscosity measurements in the field remain a great challenge (Chevrel et al., 2019). Hence, until more reliable data on active flows are available, the connections between the characteristics preserved in solidified lavas and flow dynamics can provide insight to understand the behaviour of a flow (Chevrel et al., 2013; Castruccio et al., 2013). It is worth noting that, to this date, only few studies have been published on the rheology of lavas in Mexico: one is related to dome growth dynamics at Colima volcano (Lavallée et al., 2007) and others to lava flow emplacement of different andesitic monogenetic volcanoes in the MGVF (Krauskopf, 1948; Chevrel et al., 2016b; Larrea et al., 2019).

Airborne Laser Scanning (ALS), also known as Airborne LiDAR technology (Laser Imaging Detection and Ranging), is used for the acquisition of altitude data. These topographic data define the surface in great detail and help to generate high-resolution digital terrain models (DTMs) (INEGI, 2019). Thus, ALS can be a powerful tool in volcanological studies because it allows definition of the morphological characteristics of volcanic structures, such as lava flows (Cashman et al., 2013). This technology uses an active sensor in a telemeter that emits an infrared beam from an airborne platform. This beam is deflected by a mirror perpendicularly to the airplane's trajectory, generating a series of light-pulses that upon contact with objects or the terrain reflects part of the energy of the emitted pulse back to the sensor. This results in a dense cloud of points that can be filtered to highlight vegetation, the ground's surface, or anything in between. A distinctive feature of returns in vegetated areas is that they can occur at different levels, with the last possible return occurring at ground level (INEGI, 2019).

ALS has been used successfully for volcanological purposes elsewhere in the world (e.g. Deardorff and Cashman, 2012; Cashman et al., 2013; Dietterich and Cashman, 2014; Deligne et al., 2016; Dietterich et al., 2018; Hunt et al., 2019; Younger et al., 2019). In recent years, ALS has also proven useful for archaeological studies in Mexico, especially in areas of dense vegetation cover, where spectacular findings

have revealed extensive monumental architecture of the Maya (e.g. Inomata et al., 2020; McAnany, 2020) and Tarascan (e.g. Chase et al., 2012; Fisher and Leisz, 2013; Fisher et al., 2017; Forest et al., 2018) civilizations. In our study area, a LiDAR image has provided detailed information on the extent of the archaeological site of Angamuco (Fisher and Leisz, 2013; Fisher et al., 2017) and the topographical features of the landscape derived from past anthropogenic activity (Fig. 2A). Angamuco was erected on the lava flows of Rancho Seco volcano and is now hidden under a dense mixed oak/pine forest cover.

In the present work, we take advantage of the high-resolution ALS products created for archaeological purposes, but which also turned out to be very useful for highlighting details of the lava flow morphology, which are not distinguishable in conventional digital elevation models (DEMs) (Figs. 2B, C). Note that contrary to Fig. 2B, in Fig. 2C only the most prominent lava flow fronts and margins are recognizable. This case represents an ideal candidate for this study, because of the geological "youthfulness" of the lava flows and associated excellent preservation of their morphological characteristics.

3. Methods and data sets

3.1. GIS and high-resolution LiDAR topography: Map and lava volume estimates

The lava flow sequence map in Fig. 3 was developed using QGIS software and topographic chart information, digital elevation models with a resolution of 5 m from INEGI (2019), and Google Earth (2002–2018) satellite images. A 50-cm-high-resolution LiDAR image acquired for the "Legacies of Resilience": The Lake Pátzcauro Basin Archaeological Project (LORE-LPB) (e.g., Fisher and Leisz, 2013; Fisher et al., 2017) was used to further improve a previously published map in Ramírez-Uribe et al. (2019). The different lava flows were delimited and colour-coded to indicate their chronological emplacement order (Fig. 3). This was accomplished by analysing their morphology and contacts between units as observed in a GIS database (LiDAR images, INEGI DEMs, and satellite images) and field observations (lava flow contacts and stratigraphic positions). Several campaigns were undertaken to

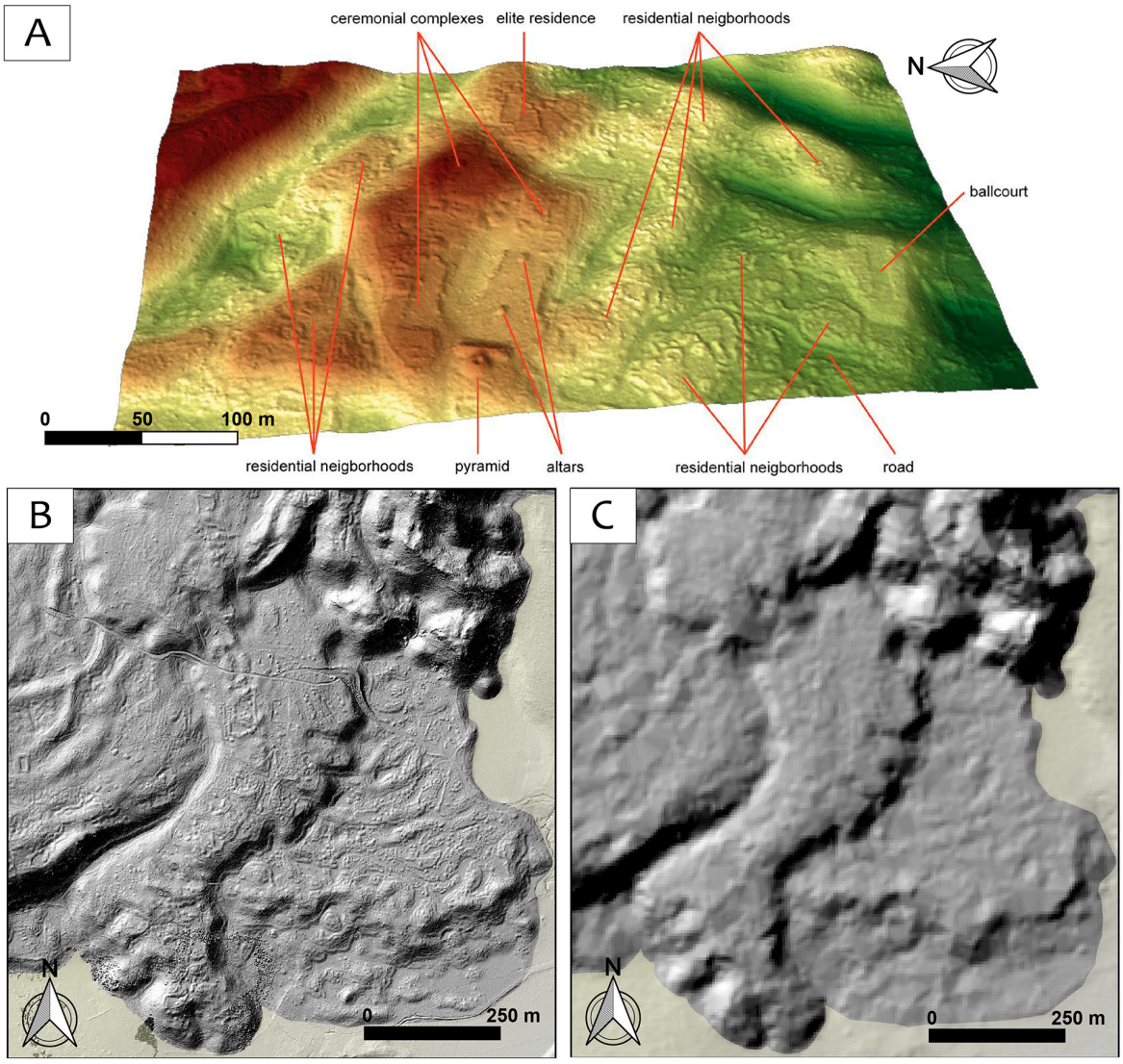

Fig. 2. A. Architectural features of the Angamuco archaeological site visible on the high-resolution LiDAR topography image (from Fisher and Leisz, 2013). B. Hillshade-DEM generated from the LiDAR image (50 cm resolution) showing distal lava flow lobes of the Rancho Seco volcano. Note that the original flow morphology was modified and adapted by ancient dwellers for constructing urban compounds. C. Hillshade-DEM (terrain type) of the same area shown in B, but based on 1:10,000 topographic data (5 m resolution) publicly available from INEGI (2019). Note that contrary to B, only the most prominent lava flow fronts and margins are recognizable. Areas covered by these images are shown on map (Fig. 3).

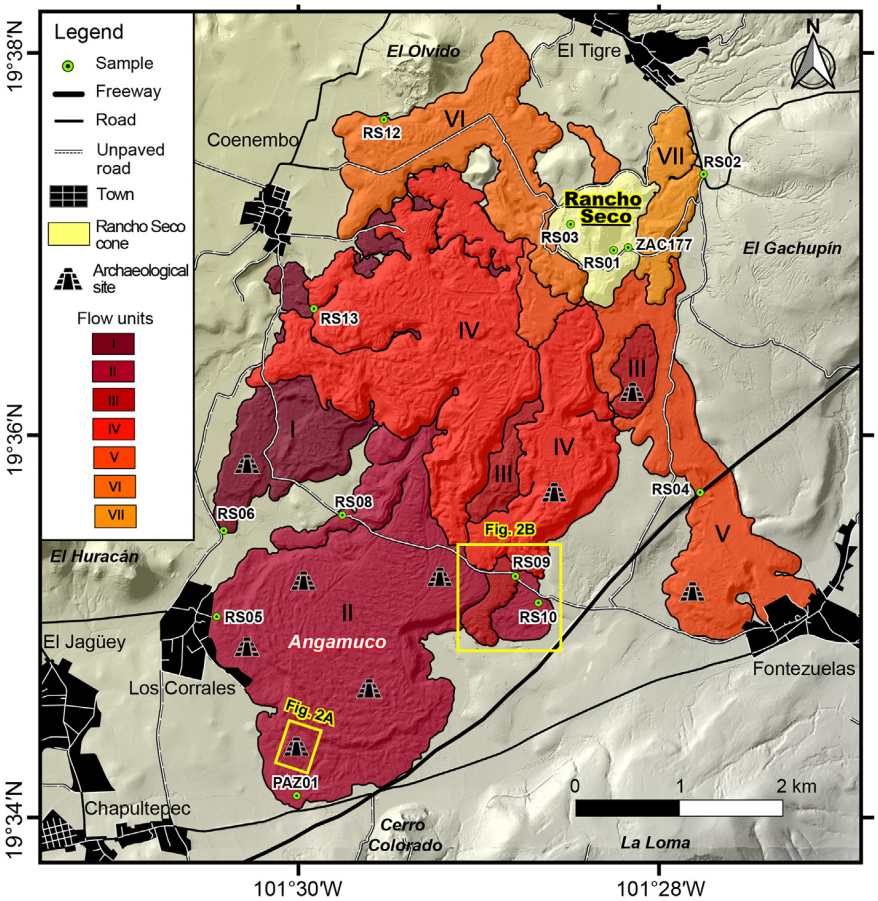

Fig. 3. LiDAR-based DEM of Rancho Seco volcano showing the sequence of its different lava flows (I-VII). Sample locations and volcanic structures on the periphery are also indicated. Yellow rectangles denote areas shown in Fig. 2A and B. (For interpretation of the references to colour in this figure legend, the reader is referred to the web version of this article).

ground-truth geologic units and stratigraphic relations and collect samples from the different lava flows of Rancho Seco volcano.

Because the 50-cm-high-resolution LiDAR image does not cover the entire area occupied by Rancho Seco's lava flows, lava volumes were estimated by calculating the volumetric difference between the 5-m resolution LiDAR from INEGI (2019) and a modified DEM. The surface below the lavas was reconstructed with a paleo-topography interpolated with a triangular irregular network model (TIN). The topographic relief before Rancho Seco's eruption was reconstructed interpolating the 5-m topographic lines (Fig. 4). For this, we used their most probable continuation using the surrounding topographic line patterns as a guide (methodology described in Chevrel et al., 2016a), by obtaining an irregular topography beneath the present edifice. For this we extracted the contour lines from the current DEM, and clipped out the area covered by a polygon delimiting each lava flow group. We selected two lava groups, one for all lava flows (F1-F7) and the other for well-exposed flows (F5-F7) to get more detailed volume estimates (Fig. 4B, C). Once the paleo-surface was obtained, it was subtracted from the topography "with" the lava flow. Care was taken to avoid over-estimating the volume (Fig. 4D). By this more refined procedure, the volume of the entire lava flows was calculated to be 0.72 km^3, in contrast to an earlier estimation of 0.64 km^3 by Ramírez-Uribe et al. (2019). These data were required for the estimation of the total emplacement time of all of the lavas. In the case of individual flows F5 and F6, we considered a simplified geometry (average thickness, flow width, and length) for each flow by making topographic profiles perpendicular to the main flow direction and obtained volumes of 0.05 and 0.06 km^3, respectively. It is important to note that by using this methodology without considering the paleo-topography, a total volume for all flows of 0.97 km^3 was estimated, which would represent the maximum volume.

3.2. Petrography and chemical analyses

Rock samples were collected from each lava flow front, as well as from the scoria cone (Fig. 3). Petrographic analysis was used to characterize their mineralogical properties and to estimate modes. Modes were estimated with point counting using 1000 points per thin-section; modal proportions of phenocrysts (≥0.3 mm), microphenocrysts (<0.3–0.15 mm), microlites (<0.15 mm), vesicles, as well as glass were calculated (Table 1).

Chemical analyses (major and trace elements; Appendix 1) were carried out at Activation Laboratories Ltd. (Actlabs), Ancaster, Canada and analytical methods included Fusion-Inductively Coupled Plasma (FUS-ICP), Total Digestion-Inductively Coupled Plasma (TD-ICP), and Instrumental Neutron Activation Analysis (INAA). For more information about the analytical procedures see the Activation Laboratories website (http://www.actlabs.com) and Agustín-Flores et al. (2011).

Mineral and glass compositions were determined using an electron microprobe (JEOL JXA-8230 Superprobe) at the Microanalysis Laboratory of the Instituto de Geofísica, UNAM, Campus Morelia. Selected thin sections were vacuum carbon-coated. The measuring conditions were an accelerating voltage of 15 kV and a beam current of 10 nA (with a diameter of 1 μm), and the counting times were 40 s for Ti, Fe, and Mg, and 10 s for K, Na, Ca, Si, and Al. Element measurements were

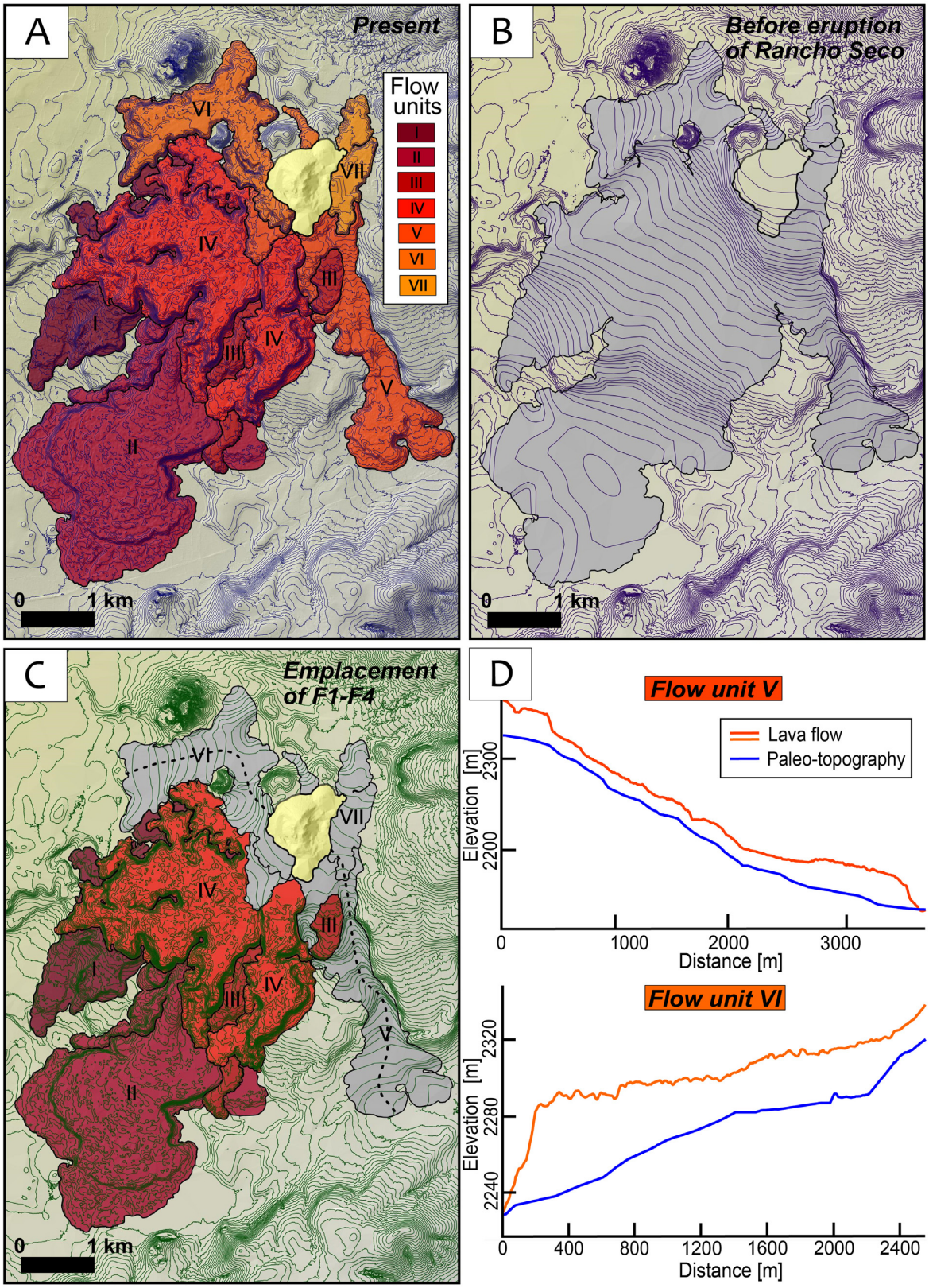

Fig. 4. Digital elevation model of Rancho Seco volcano area showing (A) the present topography, (B) a hypothetical reconstruction of the topography before its eruption (~27,845 +445/−425 years BP), and (C) a hypothetical reconstruction of the topography after emplacement of flow units I-IV. D. Topographic profiles (in flow direction) across well-exposed Rancho Seco lava flows (F5 and F6) with their paleo-topography. Profile lines are shown in C.

Table 1
Modal mineralogical analyses of Rancho Seco volcano rock samples.

Sample	Phenocrysts[a]			Micro-phenocrysts + microlites[a,b]				Gls	Vs	Total
	Plg	Opx	Qtz	Plg	Opx	Cpx	Op			
PAZ-01	0.4%		0.2%	56.0%	1.1%		1.7%	39.9%	0.7%	100%
RS-05			0.1%	56.1%	1.0%		2.2%	38.9%	1.7%	100%
RS-08	0.1%			53.8%	7.8%		1.0%	32.5%	4.8%	100%
RS-10				42.1%	14.3%	1.0%	4.2%	38.1%	0.3%	100%
RS-06	0.3%	0.2%		45.1%	10.1%	0.5%	3.7%	38.9%	1.2%	100%
RS-09				55.4%	13.9%		4.5%	24.3%	1.9%	100%
RS-13	0.2%	0.2%		57.2%	12.1%		3.6%	25.8%	0.9%	100%
RS-04				54.8%	10.5%		3.8%	30.1%	0.8%	100%
RS-12				58.0%	10.2%		8.5%	22.0%	1.3%	100%
RS-02	0.2%			66.2%	4.1%		1.6%	25.9%	2.0%	100%
RS-01				41.5%	1.0%		1.2%	43.4%	12.9%	100%
RS-03	0.1%			49.2%	2.0%		1.4%	47.3%		100%
ZAC-177				31.6%	1.5%		2.0%	50.7%	14.2%	100%

[a] Abbreviations: Plagioclase (Plg), orthopyroxene (Opx), clinopyroxene (Cpx), quartz (Qtz), opaque minerals (Op), glass (Gls), and vesicles (Vs). Phenocrysts (≥0.3 mm), micro-phenocrysts (<0.3–0.15 mm) and microlites (<0.15 mm).
[b] Most of the percentage corresponds to microlites, as the micro-phenocrysts are scarce.

calibrated from a variety of reference mineral standards, which were: PETL (rutile) for Ti, LIFL (fayalite) for Fe, PETJ (orthoclase) for K, TAP (albite) for Na, PETJ (diopside) for Ca, TAP (orthoclase) for Si, TAP (albite) for Al, and TAP (diopside) for Mg. In addition, backscattered-electron (BSE) images were obtained to observe details of the different mineral phases that could not be seen under the polarizing microscope. The average compositions of the glass and rock minerals in Rancho Seco samples are listed in Table 2.

Table 2
Average compositions of glass and minerals in rocks from Rancho Seco volcano.

	Sample	Flow unit	SiO_2 (wt. %)	TiO_2 (wt. %)	Al_2O_3 (wt. %)	FeO (wt. %)	MnO (wt. %)	MgO (wt. %)	CaO (wt. %)	Na_2O (wt. %)	K_2O (wt. %)	Cr_2O_3 (wt. %)	Total	*n**
Glass														
	RS-03	Bomb	68.81	1.36	14.93	3.38	0.1	0.46	2.91	5.08	2.97	n.a.	100.0	2
		*stdev**	*0.24*	*0.002*	*0.14*	*0.24*	*0.01*	*0.18*	*0.04*	*0.08*	*0.19*			
Plagioclases														
Rim	RS-06	1	53.35	0.06	29.31	0.9	n.a.	0.07	11.5	4.56	0.25	n.a.	100.0	3
		*stdev**	*1.88*	*0.02*	*0.98*	*0.11*		*0.02*	*1.3*	*0.61*	*0.07*			
Rim	RS-10	2	54.42	0.09	28.67	0.89	n.a.	0.07	10.87	4.59	0.4	n.a.	100.0	5
		*stdev**	*0.75*	*0.02*	*0.56*	*0.07*		*0.01*	*0.49*	*0.19*	*0.08*			
Rim	RS-09	3	54.42	0.07	28.62	0.79	n.a.	0.07	11.06	4.59	0.37	n.a.	100.0	10
		*stdev**	*0.83*	*0.02*	*0.52*	*0.11*		*0.01*	*0.65*	*0.43*	*0.06*			
Rim	RS-13	4	54.55	0.09	28.56	0.9	n.a.	0.07	10.59	4.83	0.4	n.a.	100.0	5
		*stdev**	*1.74*	*0.02*	*1.09*	*0.05*		*0.02*	*1.02*	*0.51*	*0.15*			
Rim	RS-04	5	54.42	0.08	28.67	0.83	n.a.	0.06	10.82	4.78	0.34	n.a.	100.0	4
		*stdev**	*0.35*	*0.01*	*0.28*	*0.05*		*0.01*	*0.36*	*0.18*	*0.06*			
Rim	RS-12	6	53.73	0.07	29.04	0.91	n.a.	0.06	11.19	4.67	0.34	n.a.	100.0	3
		*stdev**	*0.25*	*0.01*	*0.65*	*0.06*		*0.01*	*0.05*	*0.23*	*0.01*			
Rim	RS-02	7	54.73	0.09	28.39	0.83	n.a.	0.09	10.75	4.71	0.41	n.a.	100.0	4
		*stdev**	*2.57*	*0.03*	*1.63*	*0.1*		*0.01*	*1.59*	*0.61*	*0.2*			
Orthopyroxenes														
Rim	RS-06	1	53.15	0.33	3.11	15.18	0.34	25.89	1.89	0.1	n.a.	n.a.	100.0	8
		*stdev**	*0.67*	*0.09*	*1.73*	*3.77*	*0.12*	*2.99*	*0.37*	*0.10*				
Rim	RS-10	2	53.07	0.42	1.41	19.14	0.44	23.57	1.91	0.03	n.a.	n.a.	100.0	4
		*stdev**	*0.6*	*0.1*	*1.21*	*3.7*	*0.11*	*2.92*	*0.32*	*0.01*				
Rim	RS-09	3	53.68	0.38	0.99	17.79	0.39	25.08	1.67	0.02	n.a.	n.a.	100.0	6
		*stdev**	*0.49*	*0.08*	*0.21*	*0.62*	*0.12*	*0.67*	*0.13*	*0.02*				
Rim	RS-13	4	53.25	0.32	2.59	15.36	0.36	26.62	1.47	0.03	n.a.	n.a.	100.0	7
		*stdev**	*0.82*	*0.05*	*0.73*	*2.54*	*0.08*	*1.81*	*0.2*	*0.02*				
Rim	RS-04	5	53.33	0.36	0.93	19.9	0.39	23.26	1.79	0.05	n.a.	n.a.	100.0	2
		*stdev**	*0.19*	*0.06*	*0.12*	*0.9*	*0.07*	*0.86*	*0.23*	*0.01*				
Rim	RS-12	6	53.83	0.35	1.76	15.09	0.41	26.85	1.69	0.03	n.a.	n.a.	100.0	6
		*stdev**	*0.72*	*0.05*	*0.69*	*2.44*	*0.14*	*1.63*	*0.17*	*0.02*				
Rim	RS-02	7	53.27	0.41	1.59	17.53	0.38	25.04	1.75	0.03	n.a.	n.a.	100.0	3
		*stdev**	*0.34*	*0.04*	*0.3*	*1.02*	*0.05*	*0.53*	*0.07*	*0.02*				
Clinopyroxenes														
Rim	RS-10	2	51.81	0.85	3.54	12.16	0.37	13.05	17.36	0.86	n.a.	n.a.	100.0	2
		*stdev**	*1.52*	*0.13*	*2.52*	*0.16*	*0.004*	*2.23*	*1.22*	*0.76*				
Ilmenites														
	RS-10	2	n.a.	22.39	1.51	73.04	0.5	2.2	n.a.	n.a.	n.a.	0.35	100.0	5
		*stdev**		*1.15*	*0.06*	*1.16*	*0.02*	*0.12*				*0.17*		
	RS-12	6	n.a.	20.75	1.2	75.12	0.55	1.51	n.a.	n.a.	n.a.	0.87	100.0	6
		*stdev**		*1.73*	*0.15*	*1.45*	*0.07*	*0.35*				*1.07*		

* Abbreviations: Number of points analyzed (n), standard deviation (stdev), not analyzed (n.a.)

3.3. Lava temperature, viscosity, and effusion rate

3.3.1. Thermobarometry

Lava crystallization temperatures and pressures were calculated via the orthopyroxene-liquid geothermobarometer (Beattie, 1993) and the plagioclase-liquid geothermometer (Putirka, 2005). Water contents were estimated using the plagioclase-liquid hygrometer of Waters and Lange (2015) and using temperatures from the plagioclase-liquid geothermometer and a pressure of 1 kbar. This pressure value stems from experiments on plagioclase-free andesites from the Zitácuaro area in eastern Michoacán (Blatter and Carmichael, 1998). Before applying these geothermobarometers and the hygrometer we performed equilibrium tests using the microprobe analyses of microlites and bulk rock chemical compositions (details of the methods and equilibrium tests are provided in Appendix 2).

3.3.2. Viscosity

Lava viscosity was calculated assuming a mixture of melt and crystals based on the petrographic characteristics of the samples (Appendix 3). The effect of bubbles was ignored given the low fraction of vesicles (<4.8 Vol. %). The melt phase is assumed to have Newtonian rheology and its viscosity is calculated via the model of Giordano et al. (2008) that considers temperature, major element composition, and H_2O-content. When crystallization occurs, the lava viscosity increases and rheology deviates towards non-Newtonian behaviour (Lejeune and Richet, 1995). The effect of crystals was evaluated by considering two populations of crystals simulating spheres and prolate shapes, for mafic and plagioclase crystals, respectively, and by applying the Costa et al. (2009) equations with the fitting parameters of Cimarelli et al. (2011); see Appendix 3.

Accordingly, for pre-eruptive conditions, we assumed that no crystals were present, and the viscosity is calculated using the whole rock chemical composition, and the H_2O-content and temperature as previously estimated. For *syn*-eruptive condition, we calculated the lava viscosity at the already estimated temperatures but considered the amount and shape of crystals that we obtained from petrographic analyses and an evolved melt phase. The melt phase viscosity is calculated from the groundmass-glass (interstitial liquid) composition measured from a collected bomb sample (sample RS-03) and assuming a low dissolved water content (0.1 wt. % H_2O) due to gas-exsolution at the moment of eruption.

3.3.3. Estimation of effusion rates and flow duration

Lava flow dimensions and morphologies can be interpreted to estimate average eruption rates, velocities and duration time scales. Flow dimensions (length, width, and thickness) were extracted from the

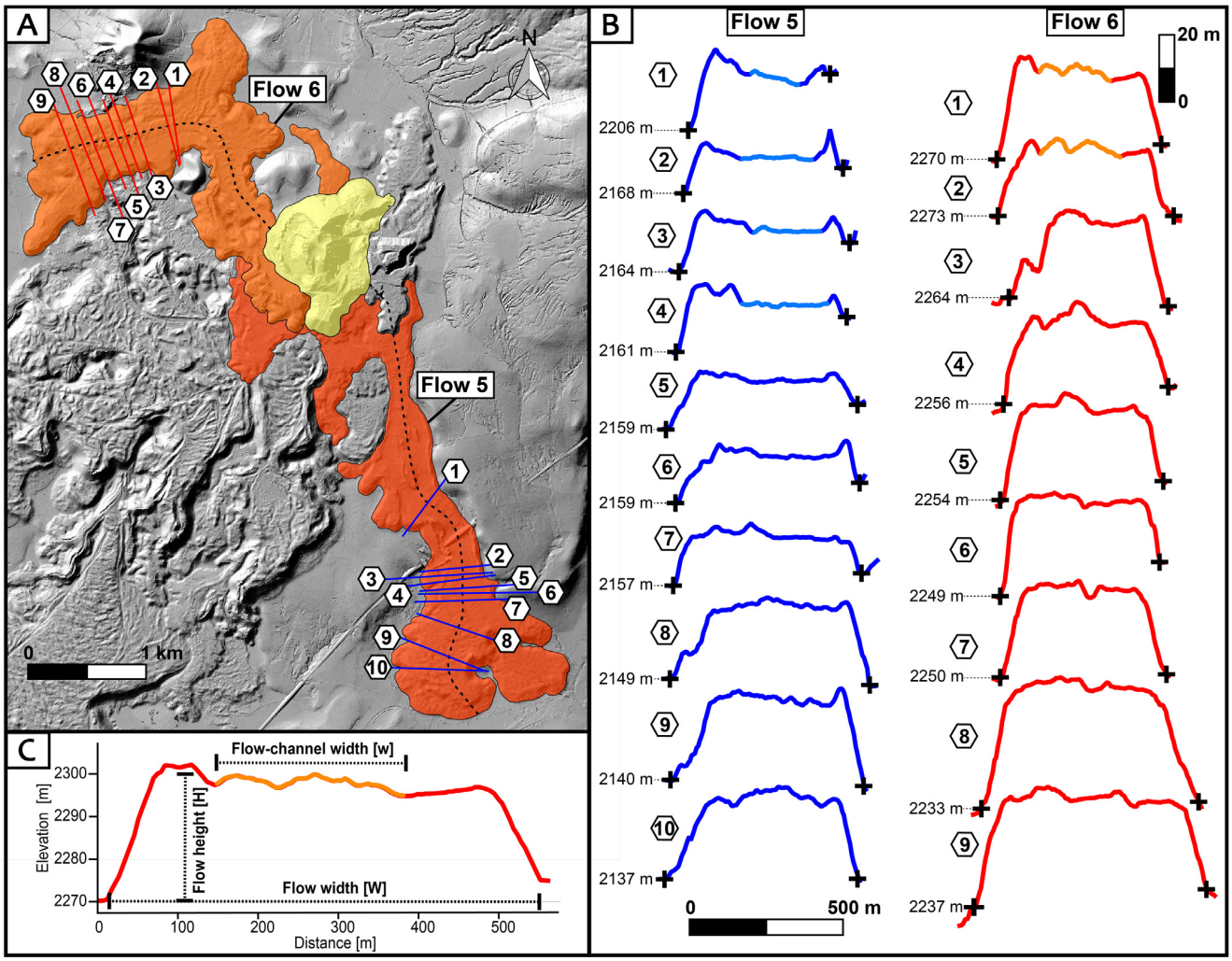

Fig. 5. A. LiDAR-DEM showing well-exposed lava flows in the study area. B. Topographic profiles (perpendicular to flow direction) across well-exposed Rancho Seco lava flows (F5 and F6) from which width, thickness, and channel width were estimated. C. Example of typical lava profile.

best exposed lavas (F5 and F6) (Appendix 4). We selected 9 to 10 profiles drawn perpendicular to the flow direction and determined flow average width and thickness, and also identified channels and levees (Fig. 5). Each profile is an average of 5 individual measurements spaced one meter apart. The topographic gradient was inferred adjacent to the lava flow where the underlying topography is exposed as well as on the flow surface simulating the pre-eruptive topography (Appendix 4).

One of the most common methods considers that the whole flow behaves as a laminar Newtonian fluid (neglecting post emplacement inflation or deflation) (Harris and Rowland, 2015) and the average flow velocity is calculated via the Jeffreys equation (Jeffreys, 1925). For this we considered an average flow thickness and the lava viscosity obtained from the sample's petrological analyses (Appendix 3). The velocity was then converted into an average effusion rate and a duration of emplacement calculated by considering the volume of the flow.

However, this simple model neglects the effect of a growing crust that may impede flow advance (Kerr and Lyman, 2007; Castruccio et al., 2013). Kerr et al. (2006) showed that the cross-slope flow distance from the channel center-line (i.e., half of the channel width) can be described as a balance between parameters that contribute to flow spreading and the restraints provided by crustal cooling (Deardorff and Cashman, 2012). Depending on the lava properties and initial conditions, Kerr and Lyman (2007) showed that lava flows may stop either by an internal yield-strength or by the yield-strength of a growing surface crust. Considering that the lava flow is controlled by the yield-strength of the growing crust, we used the equations of Kerr et al. (2006) to estimate the effusion rate (Eq. 14, Appendix 3). This assumes that the core of the lava (below the crust) is nearly crystal free and well represented by the melt viscosity (i.e. as calculated from the glass composition at the eruption temperature). The effusion rate is then converted into duration considering the volume of the flow.

Alternatively, we used three other approaches to estimate the flow emplacement duration and effusion rate without viscosity constraints. One is based on the relationship between effusion rate and flow lengths and proposes that the maximum length a flow can reach is related to its velocity (and hence effusion rate) given the amount of heat that is lost by conduction through its thickness (Walker, 1973; Pinkerton, 1987; Pinkerton and Sparks, 1976; Pinkerton and Wilson, 1994). This is represented by a dimensionless number – the Grätz-number –which is ~300 for most cooling-limited basaltic flows as determined by Pinkerton and Wilson (1994). Another approach, remodelled from Kerr et al. (2006) was proposed by Castruccio et al. (2013). This also considers that the flow is slowing down due to the yield strength of a crust that is growing by conductive cooling, and allows estimation of the duration of a flow's emplacement (Eq. 16, Appendix 3). Finally, we used the study of Kilburn and Lopes (1991) that is well adapted for thick blocky lava flows to calculate their emplacement duration based only on their final dimensions and the estimated paleo-topography (Eq. 18, Appendix 3). The results of these three viscosity-independent methods are then converted into effusion rate and velocity considering the volume of the flow.

4. Results

4.1. Lava flow morphology

Despite being covered by an oak/pine forest, the lava morphology of Rancho Seco volcano is remarkably well-preserved. The high-resolution LiDAR image allowed for more accurate mapping and has established a new emplacement sequence (Fig. 3) relative to Ramírez-Uribe et al. (2019).

The Rancho Seco volcano is a monogenetic scoria cone with a maximum elevation of ~2520 m a.s.l. (above sea level) and a height of ~200 m above surrounding ground, and an almost circular base with a diameter of ~880 m. Today, the initial crater is practically unrecognizable due to intensive quarrying of the cone (Fig. 6A). Individual lava flows radiate away from the base of the cone (Fig. 3) mainly towards the SW. They extend distances of up to 6.4 km away from the cone; shorter lavas extend towards the NW (3.5 km) and NE (1.5 km). These differences are explained by the range of underlying slopes and the occurrence of topographic barriers.

Lava flow morphology at Rancho Seco volcano is predominately of the ʻaʻā type, but some block lava flows were also recognized. In roadcuts and quarries exposing the interior, the lava is massive (dense) with well-developed basal and surface breccias. Some flows have well-defined channels, separated by stationary margins (levees) delimitated by clear shear zones that are quasi-continuous from the vent to the flow front (Fig. 6B, C). Lava surfaces within the channels exhibit surface ridges (also called ogives) perpendicular to flow direction (Fig. 6B, C), which form in response to a slowing flow front and subsequent buckling of a stiff surface-crust behind it (Fink, 1980). We also observed breakouts widely distributed on lava fronts and some margins, which represent a characteristic process in cooling-limited lava flows (Wilson and Head, 1994; Magnall et al., 2019). These are formed when the internal pressure within the lava flow exceeds the local confining force, due to increased core pressure and/or decreased crust strength (Magnall et al., 2019).

4.2. Mineralogy and petrography

All samples are andesites with low modal percentages of phenocrysts (≥0.3 mm, <0.6 Vol. %; Table 1), which show aphanitic and occasionally trachytic textures (Fig. 7A, B). Mineral phases in all lavas include mainly plagioclase and orthopyroxene, minor clinopyroxene and opaques, and rare quartz xenocrysts (Fig. 7D). In general, the groundmass contains a high content of microlites of plagioclase (<0.1 mm; 31–67 Vol. %; Table 1), which dominantly have needle-like habits with aspect ratios (length/width) between 2 and 13, while larger phenocrysts (~1 mm; <0.4 Vol. %) and micro-phenocrysts are scarce. All lava samples are characterized by a low content of vesicles (<2.5 mm; <4.8 Vol. %) while bomb samples (ZAC-177 and RS-01) contain up to 14.2 Vol. % of vesicles.

The phenocrysts usually exhibit sieve-textures and rounded margins (Fig. 7C), while others show zoning patterns and form rare glomeroporphyritic clusters. Because of these disequilibrium textures most large crystals are interpreted as being xenocrysts. Orthopyroxenes (hypersthene; Fig. 7A, B) have typical subhedral-euhedral habits and occur mainly as microlites (<0.1 mm; 1.0–14.3 Vol. %; Table 1) with aspect ratios between 1 and 2 and only rarely as phenocrysts (up to 0.8 mm; up to 0.2 Vol. %). Occasionally, they form isomorphic replacements of quartz crystals. Clinopyroxenes (augite) are extremely rare and only observed as microlites (<0.1 mm; up to 1.0 Vol. %) with subhedral-anhedral habits and dissolution rims. Opaque minerals occur as microlites and were found in all samples (<0.05 mm; 1.0–8.5 Vol. %) and are distributed in the groundmass, but also occur as inclusions in pyroxenes. Opaque crystals in the matrix are generally ilmenites (Fig. 7A). Quartz xenocrysts (up to 0.5 mm) display marked dissolution embayment textures (Fig. 7D) and occasionally thin coronas of hypersthene and plagioclase microlites. Compositions of microlites of plagioclase (Fig. 8) fall mostly in the labradorite ($An_{50–62}$), but few also in the andesine field ($An_{44–45}$). Crystal-rim compositions of orthopyroxene microlites fall in the enstatite field and display a wide range ($En_{59–79}$) in comparison to clinopyroxene microlites (~En_{40}), which plot in the augite field (Fig. 8).

4.3. Major and trace element contents

A total of 13 rock samples were analyzed chemically (Table A1, Appendix 1) and plotted in a total-alkali (Na_2O+K_2O) vs. SiO_2 diagram (Fig. 9; after Le Bas et al., 1986) to define magma types. Analytical results were normalized to 100% on an anhydrous basis before being plotted in this and subsequent diagrams (Figs. 9 and 10). All rocks fall in the andesite field (58.5–60.6 wt. % SiO_2), are sub-alkaline (Irvine and

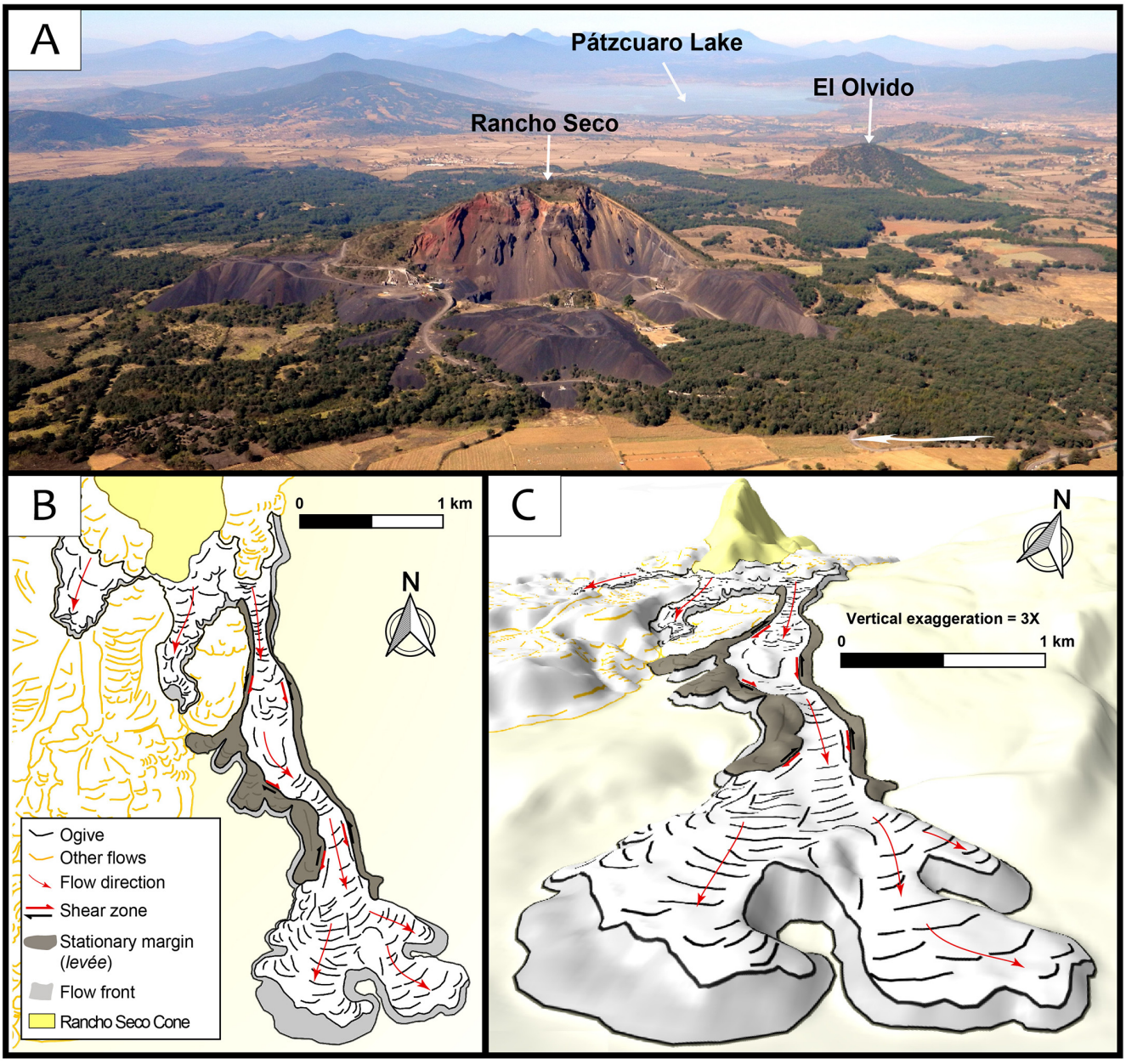

Fig. 6. A. Aerial view of Rancho Seco volcano with its diverse lava flows and peripheral topography. Note extreme degradation of the cone by intense recent quarrying. B. Schematic representation of the main characteristics of the lava flows studied. Vertical view of lava flow 5 (see Fig. 3) from Rancho Seco volcano. C. Perspective view from the SW of the main cone and lava flow 5.

Baragar, 1971), and show a medium-K calc-alkaline trend. K_2O-values (1.5–1.9 wt. %) are mostly higher in comparison to Paricutin samples. Rancho Seco samples are remarkably homogeneous in composition (Fig. 9), which contrasts with the wider evolutionary patterns displayed by other monogenetic volcanoes in the TMVB, e.g. in the Sierra Chichinautzin (Siebe et al., 2004), but also in the MGVF, where the best studied example is Paricutin volcano, whose SiO_2-contents range between 53 and 60 wt. % (Wilcox, 1954; Cebriá et al., 2011; Larrea et al., 2019).

Other major and trace elements (Ni, Sr, and Ba) were also plotted in Harker diagrams (Fig. 10) and compared with samples from Paricutin (data from Cebriá et al., 2011 and Larrea et al., 2019). Rancho Seco lavas display negative correlations for Al_2O_3, Na_2O, and Sr, generally have lower concentrations of Al_2O_3, MgO, Na_2O, and Ni, have higher K_2O, and Ba, while CaO and Sr values are similar as compared with Paricutin.

In multi-element diagrams (Sun and McDonough, 1989; McDonough and Sun, 1995), Rancho Seco patterns are similar to those of Paricutin, although a slightly higher fractionation of heavy rare earth elements (REE) is observable in the Rancho Seco rocks (Fig. 11), while Paricutin samples show a slight enrichment in the mid-REE.

Both Rancho Seco and Paricutin display typical negative anomalies of Nb, Ta, and Ti, and considerable enrichment in the large-ion lithophile elements (LILE) with respect to the high-field-strength elements (HFSE), as well as REE patterns with higher light-REE with respect to the heavy-REE, as is common in continental volcanic arcs related to subduction environments (Hawkesworth et al., 1977; Gill, 1981; Gómez-Vasconcelos et al., 2015). Many samples display a strong positive

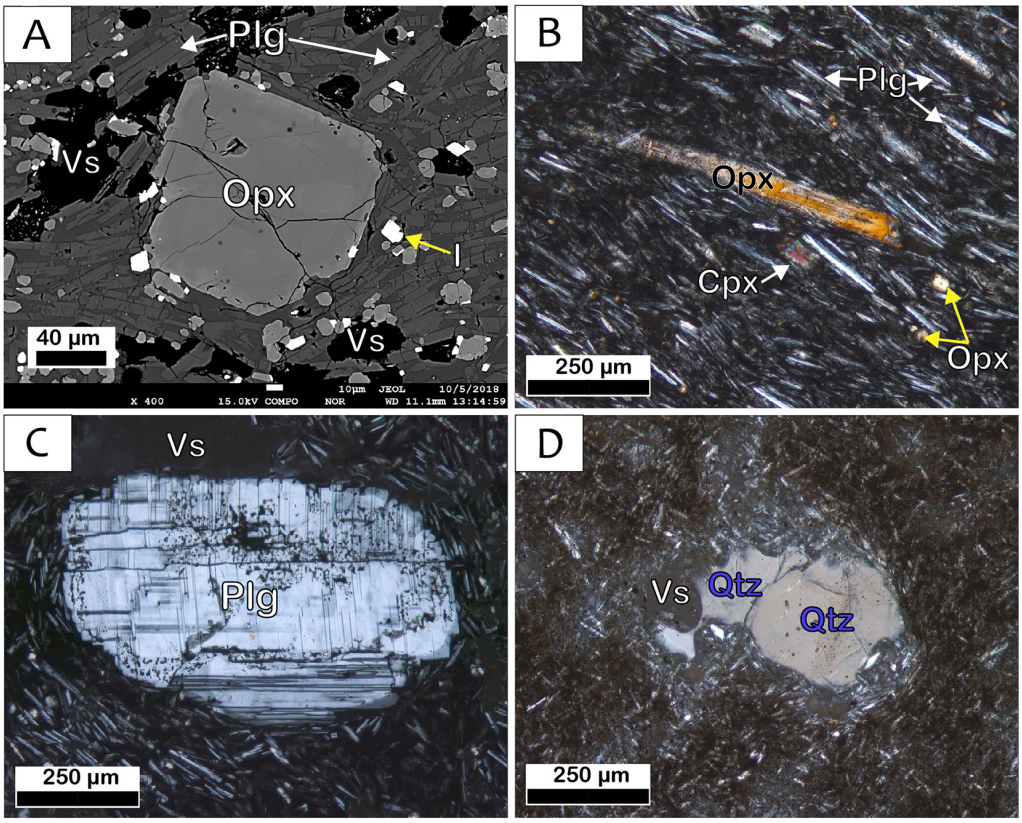

Fig. 7. A. Back-scattered electron microscope (BSE) image of a slightly zoned orthopyroxene crystal embedded in a microlite-rich matrix with a trachytic texture (sample RS-12). Photomicrographs (crossed nicols) under the petrographic microscope (B, C, and D) of Rancho Seco rock samples. B. Elongated crystal of enstatite and trachytic texture (sample RS-06). C. Partly resorbed (rounded margins) plagioclase crystal displaying sieve texture (sample RS-08). D. Quartz xenocryst with dissolution embayments (sample RS-05).

Pb-anomaly, although some samples show values below the detection limit (<5 ppm) of the analytical method (ICP-OES) and were not plotted. Rancho Seco rocks also show a less pronounced negative Rb-anomaly in comparison to Paricutin.

4.4. Thermobarometry and hygrometry

We estimated temperatures and pressures, as well as water-contents for all lava flow samples of Rancho Seco volcano (Table 3; Fig. 12). Estimated temperatures from plagioclases in the different lava flows cover a range of 1083–1093±36 °C, while orthopyroxenes indicate slightly higher temperatures in the range of 1087–1094±39 °C and pressures of 1.1–3.5±2.6 kbar corresponding to depths of 4 to 14 km. Water contents estimated using plagioclase compositions yielded a range of 1.4–1.9±0.35 wt. % H_2O. These temperatures show a narrow range, and are similar to measurements obtained directly at the active Paricutin lava flows (Krauskopf, 1948), as well as to those calculated by applying different mineral geothermometers at the andesitic El Metate volcano (Chevrel et al., 2016b).

4.5. Magma and lava rheology

At pre-eruptive conditions, the viscosity of the magma (estimated from the bulk rock composition without crystals) is estimated at 320–760 Pa·s (1086–1094 °C; 1.4–1.9 wt. % H_2O; Table 4). For these estimations, we neglected the volume of crystals because it is low (<0.6 Vol. %) and in some samples even absent (Table 1). The viscosity of the extruded (degassed) lava was then estimated at ~3×10^5 Pa·s (1086–1089 °C; 0.1 wt. % H_2O; Table 4) when considering only the evolved melt phase (no crystallization) to 4.2×10^8 and 1.9×10^9 Pa·s when considering 56–70 Vol. % of microlites and the Costa et al. (2009) model (Table 4). Considering that many of the samples have a trachytic texture, i.e. the crystals are oriented in a preferential direction, we calculated the viscosity for a high deformation rate of 1 s^{-1} (Cimarelli et al., 2011). Error propagation (Appendix 5) for these models (calculated according to standard deviation of our temperature estimates) yields an error of up to 20%.

4.6. Effusion rate and emplacement duration

All morphological flow parameters are given in Table 5 and in this section we present a summary of the effusion rates, velocities, and emplacement times of the Rancho Seco lava flows as calculated by morphology-based methods (Table 6). Using the lava viscosity from the petrological analyses of the lava flow front samples (η_{F5}= 1.1×10^9 and η_{F6}= 1.3×10^9 Pa·s; Table 4) and the Jeffreys (1925) equation (Eq. 9, Appendix 3), the measured flow thickness, a slope of ~1° and ~3° and a density of 2565 kg/m^3, the flow velocity would be 16 and 19 m/day for F5 and F6, respectively. Considering the volume of the flow obtained from their average width and their length (5.2×10^7 and 6.2×10^7 m^3 for F5 and F6, respectively), this converts into an effusion rate of 2 and 5 m^3/s and an emplacement duration of 250 and 137 days for F5 and F6, respectively.

Alternatively, the effusion rate can be obtained through the Grätz-number approach (Eq. 12, Appendix 3; Pinkerton and Sparks, 1976; Hulme and Fielder, 1977). Results yielded effusion rates of ~5 and ~13 m^3/s for F5 and F6, respectively. This can be converted into emplacement durations of 47 and 138 days which correspond to lava advances of 19 and 84 m/day for F5 and F6, respectively.

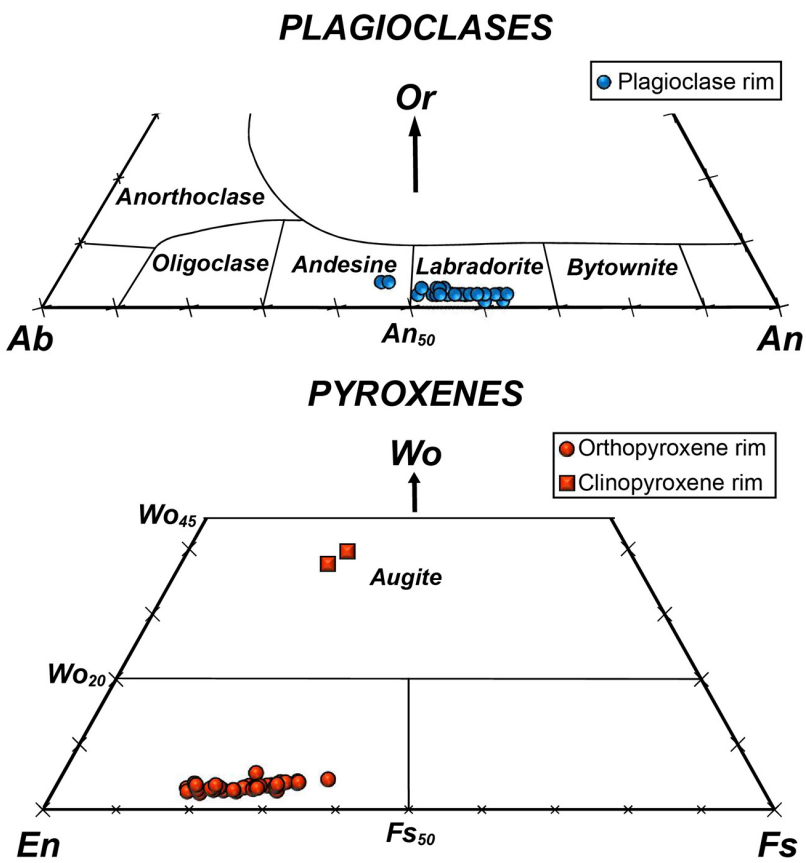

Fig. 8. Composition of plagioclases (Ab-An-Or) and pyroxenes (Wo-En-Fs).

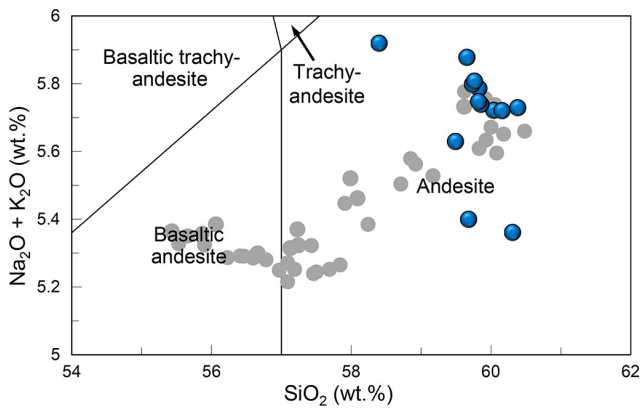

Fig. 9. Rancho Seco rock-sample compositions (blue circles) plotted in a total alkali vs. silica diagram (analyses recalculated to 100% on a H_2O-free basis) after Le Bas et al. (1986). Paricutin volcano samples (gray circles, data from Cebriá et al., 2011 and Larrea et al., 2019) are shown for comparison. (For interpretation of the references to colour in this figure legend, the reader is referred to the web version of this article).

If the flow dynamics are controlled by the effect of a growing crust we can estimate the effusion rate using the equation given by Kerr et al. (2006) (Eq. 14, Appendix 3) by assuming a yield strength of the crust (σ_c) of 2×10^6 Pa (best fit of Kerr and Lyman, 2007) and the viscosity of the lava flow core, that is the not yet crystallized lava (minimum values at *syn*-eruptive conditions: $\eta F5 = 3.1\times10^5$ and $\eta F6 = 2.9\times10^5$ Pa·s; Table 4). Results gave effusion rates of 6 and 2 m^3/s, which were converted into flow velocities of 39 and 6 m/day, and emplacement durations of 101 and 464 days for F5 and F6, respectively.

For comparison, by following the equation proposed by Castruccio et al. (2013), and assuming a yield strength of the crust (σ_c) of 3×10^5 Pa (best fit of Castruccio et al., 2013), we obtained emplacement durations of 110 and 211 days for F5 and F6, respectively (Eq. 16, Appendix 3). These convert into flow velocities of 12 and 36 m/day and effusion rates of 3 and 5 m^3/s.

Finally, we applied the model of Kilburn and Lopes (1991) (KL) and obtained emplacement durations of 32 days for F5 and 75 days for F6 (which can also be converted into effusion rates of 19 and 10 m^3/s and advancement velocities of 34–123 m/day). Error propagation (Appendix 5) for these models (calculated following Chevrel et al., 2013, Appendix A.2, see also Chevrel et al., 2016b and Lefler, 2011) yields an error of up to 19%.

5. Discussion

5.1. Magma source and evolution

The andesitic rocks of Rancho Seco volcano originated probably from a primary basaltic melt (as postulated for other volcanoes in the MGVF, e.g. Rasoazanamparany et al., 2016; Corona-Chávez et al., 2006; Osorio-Ocampo et al., 2018; Ramírez-Uribe et al., 2019) that derived from the partial melting of a heterogeneous mantle wedge (e.g. Larrea et al., 2019) metasomatized by aqueous fluids (our studied rocks reveal marked enrichments in LILE with respect to HFSE, Fig. 11B) from the subducting oceanic plate. Probably, during its ascent through the crust this magma experienced fractional crystallization and minor shallow

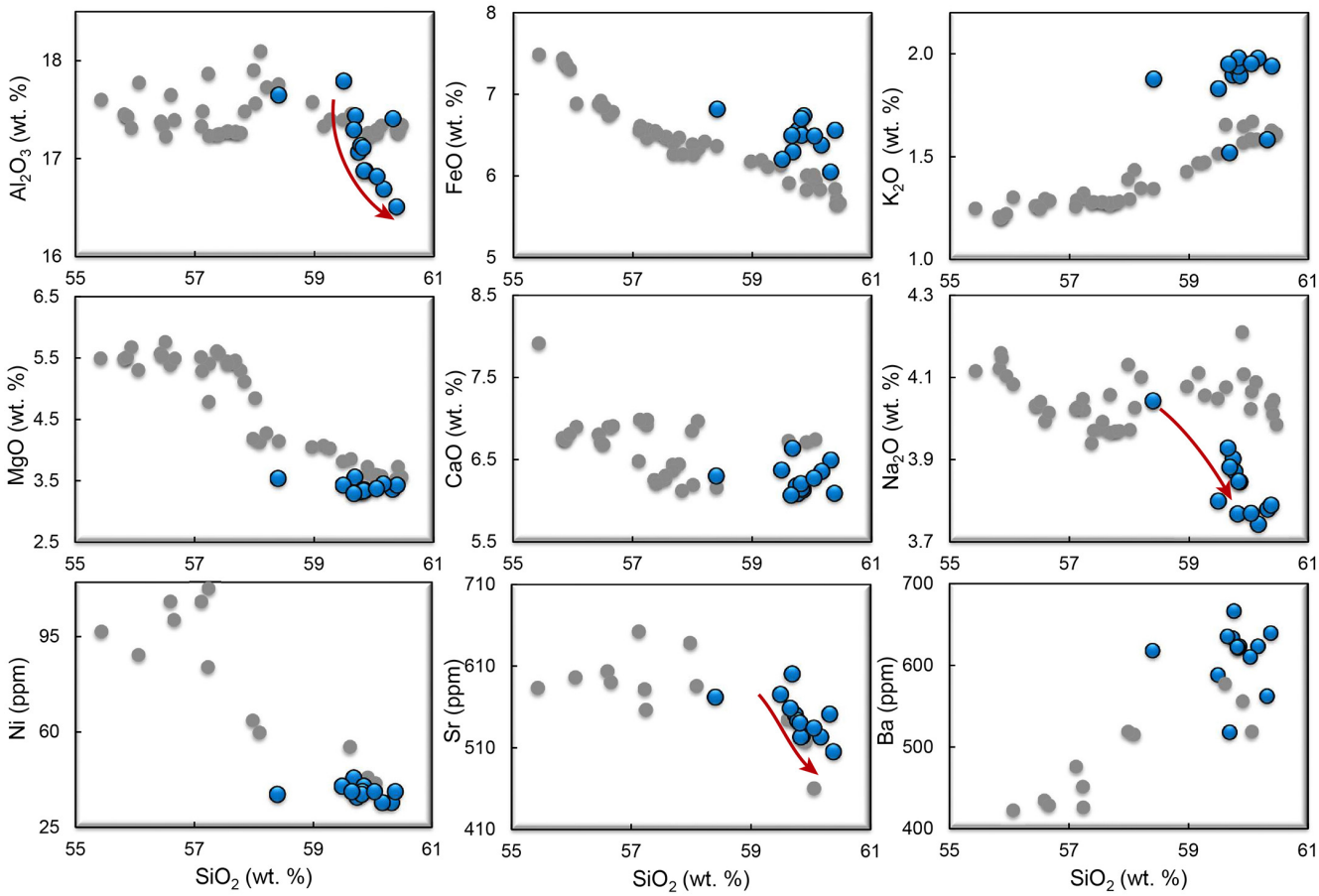

Fig. 10. Harker diagrams showing selected major (wt. %) and trace (ppm) elements plotted against silica (symbols and data sources as in Fig. 9). Red arrows represent the eruption progress. (For interpretation of the references to colour in this figure legend, the reader is referred to the web version of this article).

contamination by assimilation of plutonic granodioritic rocks, as suggested by the presence of quartz xenocrysts. The latter is also hinted by the occurrence of plutonic xenoliths reported from other lavas in the MGVF (Wilcox, 1954; Luhr and Carmichael, 1985; Verma and Hasenaka, 2004; Corona-Chávez et al., 2006). An alternative hypothesis involves an andesitic melt generated by a magma mixing: For example, Gómez-Tuena et al. (2018) propose that TMVB andesites might have a hybrid nature acquired at mantle depths through the reaction of felsic slab-derived melts with mantle peridotites or magmas made of mixtures between mantle and pre-existent crust. In this case, for hydrous intermediate magmas to erupt on the surface with such low phenocryst abundances (<0.6 Vol. %), rapid ascent through the entire crust would be required (Crabtree and Lange, 2011).

5.2. Eruptive dynamics

Rancho Seco products have relatively narrow variations of SiO_2 and other major and trace elements and all were derived from a single batch of magma that was gradually erupted. According to stratigraphy, the Rancho Seco eruption followed a pattern of activity that was similar to that observed at Paricutin volcano (Fig. 13; see also Luhr and Simkin, 1993; Pioli et al., 2008): Initial stages of violent-Strombolian activity (effective degassing of the magmatic system) produced fallout of scoria, bombs, and ashes around the crater, leading to the rapid construction of a cone (Fig. 13A; Ramírez-Uribe et al., 2019) and were followed by a largely effusive stage that successively formed a lava flow field (Fig. 13B). During the effusive stage, Strombolian activity (well-bedded ash fallout) had greatly diminished and occurred only intermittently during brief phases, since most lava flows lack an ash cover.

The change of eruption dynamics from Strombolian to effusive is likely due to efficient degassing of the magma during the Strombolian phase which led to an open system through which further degassed magma could rise through the upper crust to the surface. Nonetheless, Nguyen et al. (2014) indicate that degassing by itself is not always sufficient to promote the transition to effusive activity, which could also be a consequence of larger changes in the magma ascent rates. The change from explosive to effusive activity might therefore also be caused by a decrease in the magma ascent rate, and hence in the decompression rate. A combination of slow ascent or decompression and efficient gas-loss promotes effusive activity (Fig. 13B; Nguyen et al., 2014), which could have occurred during the effusive stage of Rancho Seco volcano. Indeed, plagioclase microlites similar to those in our samples are formed during degassing of the magma on eruption and slow decompression promotes their crystallization (Couch et al., 2003). This means that many microlites probably formed near the surface.

5.3. Lava and flow viscosity

The best historical analogue for Rancho Seco volcano might be the eruption of Paricutin (e.g. Larrea et al., 2017), since both share several similarities (e.g. size of areas covered by lava flows, maximum lava lengths, lava types, eruptive styles, etc.), but also the case of the 1988–90 Lonquimay eruption in Chile (phenocrysts-poor andesite with 58–59 wt. % SiO_2; Naranjo et al., 1992). The Rancho Seco lava

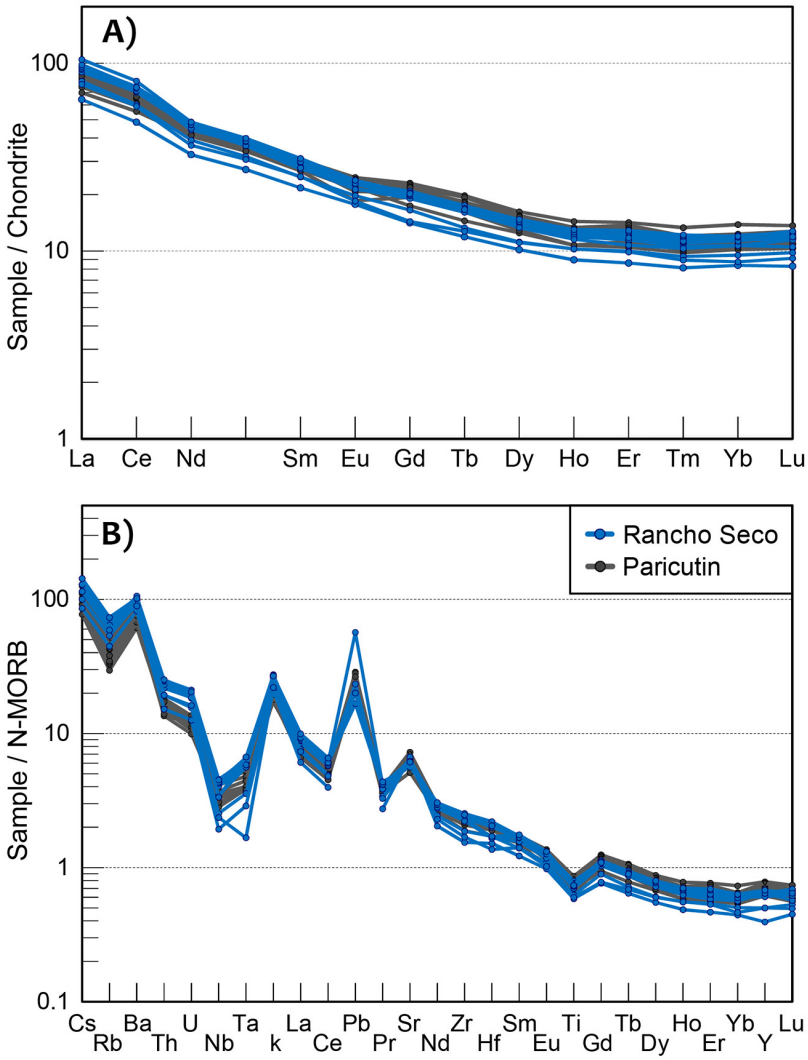

Fig. 11. A. Chondrite-normalized rare earth element (REE) plot (after McDonough and Sun, 1995) for Rancho Seco rock samples. B. N-MORB trace element patterns (after Sun and McDonough, 1989) for Rancho Seco rock samples. Rancho Seco samples are shown in blue and Paricutin samples in gray, for comparison. (For interpretation of the references to colour in this figure legend, the reader is referred to the web version of this article).

viscosities estimated from the petrography during flow emplacement (10^5–10^9 Pa·s) are close to those obtained for El Metate (Chevrel et al., 2016b) and the 1988–90 Lonquimay lavas (Castruccio and Contreras, 2016). However, it is important to note these viscosity estimates derived from petrological parameters are first-order approximations because they do not take into account heterogeneities in the distribution of crystals and bubbles, crystal interactions, etc. (Caricchi et al., 2007; Costa et al., 2009; Lavallée et al., 2007; Chevrel et al., 2016b). The increase in viscosity is attributed to the initial disequilibrium conditions of the magma at the vent with further degassing and cooling triggering crystallization of the lava flow (Castruccio et al., 2013). However, it is extremely difficult to know the amount of

Table 3
Thermo-barometry and hygrometry calculation results for Rancho Seco volcano.

Sample	Flow unit	Plagioclase-liquid[a] (Eq. 24a from Putirka 2008) and hygrometer (Waters and Lange, 2015)							Orthopyroxene-liquid[a] (Eq. 28a and 29a from Putirka 2008)					
		n	Liquid composition	T [°C]	stdev	P [kbar][b]	wt. % H_2O	stdev	n	Liquid composition	T [°C]	stdev	P [kbar]	stdev
RS-06	1	1 (Rim)	Whole rock	1087		1.0	1.9		4 (Rim)	Whole rock	1094	3.2	3.5	0.6
RS-10	2	3 (Rim)	Whole rock	1089	1.7	1.0	1.6	0.0	1 (Rim)	Whole rock	1087		2.7	
RS-09	3	6 (Rim)	Whole rock	1086	3.4	1.0	1.7	0.05						
RS-13	4	2 (Rim)	Whole rock	1089	5.2	1.0	1.4	0.07	4 (Rim)	Whole rock	1089	12.5	1.1	0.8
RS-04	5	4 (Rim)	Whole rock	1086	2.0	1.0	1.7	0.0						
RS-12	6	3 (Rim)	Whole rock	1093	1.7	1.0	1.4	0.0	3 (Rim)	Whole rock	1089	8.9	2.1	0.6
RS-02	7	1 (Rim)	Whole rock	1088		1.0	1.6							

Abbreviations: Number of points analyzed (n), temperature (T), pressure (P) and standard deviation (stdev).
[a] Equilibrium data associated with crystals are reported.
[b] Pressure data of 1.0 kbar obtained from experimentation with plagioclase-free andesites from Zitácuaro, Michoacán (Blatter and Carmichael, 1998).

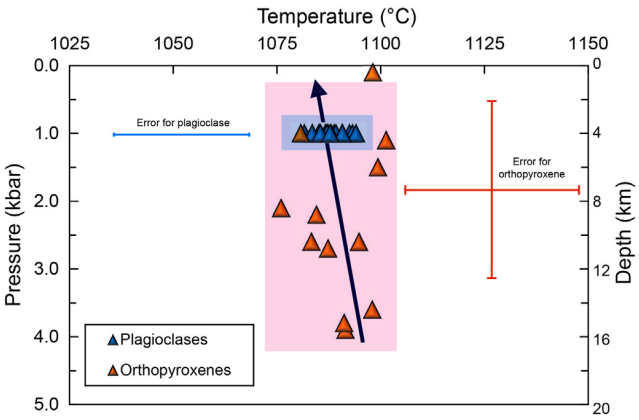

Fig. 12. Pressure-temperature diagram showing results obtained by the different geothermometers and geothermobarometers applied in this study, indicating also their uncertainties.

microlites present before the eruption and to discern between microlites that formed due to decompression in the upper part of the conduit from those formed during lava flow emplacement, and/or those formed after lava flow settlement. Since lava viscosity increases through emplacement due to cooling and crystallization (Crisp et al., 1994), our results correspond to a minimum viscosity (10^5 Pa·s) at the beginning of the eruption while the maximum values (10^9 Pa·s) represent the maximum viscosity at the rheological cut-off (Chevrel et al., 2013; Kolzenburg et al., 2017). It is interesting to show that if we estimate the flow viscosity via the Jeffreys equation (Eq. 19, Appendix 3) using the velocities obtained via the equation of Castruccio et al. (2013), the Grätz number, and the model of Kilburn and Lopes (1991), we obtained values ranging from 1.4×10^8 to 2.0×10^9 Pa·s (Table 7), which are all very similar to those obtained by the petrographic method when considering the highest amount of microlites. This reveals (as shown earlier by Chevrel et al., 2013), that for cooling-limited flows, the viscosity obtained from the morphological method is roughly equivalent to the values at the rheological cut-off that can be obtained from the petrography of the samples.

In regard to these viscosity estimates, Rancho Seco values are however higher than those estimated for the Paricutin andesitic flows with the Jeffreys equation during emplacement (see Krauskopf, 1948), but fall in the range of the 1988–90 Lonquimay andesitic flow estimates (see Naranjo et al., 1992).

In addition, where the levees were clearly identified, we could also apply the equations of Hulme (1974), which describe ideal unconfined Bingham-type flows on an inclined plane, to extract the flow viscosity (Eq. 22, Appendix 3) and yield-strength (Eq. 21, Appendix 3). Using the velocity obtained via the equation of Castruccio et al. (2013), Grätz number, and by the Kilburn and Lopes (1991) approach, flow viscosities range between 5.3×10^4 and 3.8×10^6 Pa·s and yield-strengths between 5.6×10^3 Pa and 1.9×10^4 Pa (Table 7). These values are within the same order of the minimum viscosity that we obtained from our petrographic analyses (10^5 Pa·s). Moreover, these estimates are much closer to the values obtained for Paricutin volcano and fall in the range of the andesitic lavas from El Metate volcano (Chevrel et al., 2016b).

5.4. Flow emplacement conditions and duration of eruption

From the effusion rates and the emplacement times obtained for the two flows (Table 6), we can obtain a rough notion of the approximate total time during which Rancho Seco's entire lava volume (0.72 km^3) was emplaced. To do so, we do not consider pauses that might have occurred, and also assume that each flow was erupted one after the other, and not simultaneously. The successive emplacement of all flows probably took from 2 (using a mean maximum effusion rate of 15 m^3/s from the Kilburn and Lopes model) to 6 years (using a mean minimum effusion rate of 4 m^3/s from the yield strength in a growing crust regime). We believe that the latter might be a more realistic time value considering that the occurrence of breakouts and ogives indicates the presence of a surface crust (Tuffen et al., 2013; Farquharson et al., 2015; Magnall et al., 2017). Breakouts could even indicate a transition to a core-controlled flow advance in the flow front (Carr et al., 2019). The mean mass eruption rate was estimated at 9.6×10^3–3.6×10^4 kg/s, considering a density of andesitic lava of 2565 kg/m^3 (Tenzer et al., 2011) and the average of the effusion rate values obtained by the yield strength in a growing crust regime approach (4 m^3/s), which are remarkably similar. The effusion rates and emplacement times for the analyzed flows from Rancho Seco volcano are very similar to the data reported for Paricutin (Larrea et al., 2017), while El Metate has much higher values, which is in part due to the much larger erupted lava volumes (Chevrel et al., 2016a, 2016b). In this context it should be mentioned that the Paricutin mass eruption rate declined over time while the dominant eruptive style changed from explosive (total mass eruption rate $\geq10^4$ kg/s) to mainly effusive (total mass eruption rate $<10^4$ kg/s) during the course of its activity (Pioli et al., 2009). Hence, our value for Rancho Seco falls near the limit between both eruptive styles.

The estimated mean lava flow velocities of 18–79 m/day indicate that lava fronts did advance relatively slowly and would not represent a great danger for onlooking populations. However, depending on the location of a possible future vent, a similar eruption could cause great damage to local infrastructure, as observed in the case of Paricutin. The Paricutin eruption (1943–1952) lasted much longer (>9 years), and its total erupted volume of 1.7 km^3 (Larrea et al., 2017) was roughly two times larger. Our volume estimate for Rancho Seco represents only 7% of the total lava volume of El Metate shield volcano (~10.8 km^3), for

Table 4
Magma and lava viscosities estimated by following the petrological approach.

Sample	Flow unit	Pre-eruptive condition					*Syn*-eruptive condition (0.1 wt. % H_2O)						
		T (°C)	stdev	wt. % H_2O	Melt viscosity (Pa·s)	% error*	T (°C)	stdev	Melt viscosity (Pa·s)	% error*	Relative viscosity	Lava viscosity (Pa·s)	% error*
RS-06	1	1094	3.2	1.9	3.24E+02	5.0	1087		3.02E+05		1.59E+03	4.80E+08	
RS-10	2	1089	1.7	1.6	5.37E+02	2.8	1087		2.88E+05		1.44E+03	4.15E+08	
RS-09	3	1086	3.4	1.7	5.37E+02	5.5	1086	3.4	3.09E+05	7.9	4.18E+03	1.29E+09	7.9
RS-13	4	1089	5.2	1.4	7.59E+02	8.7	1089	5.2	2.88E+05	11.9	4.49E+03	1.29E+09	11.9
RS-04	5	1086	2.0	1.7	5.25E+02	3.2	1086	2	3.09E+05	4.6	3.54E+03	1.09E+09	4.6
RS-12	6	1093	1.7	1.4	7.08E+02	2.8	1089	8.9	2.88E+05	20.4	4.46E+03	1.29E+09	20.4
RS-02	7	1088		1.6	5.62E+02		1088		2.95E+05		6.59E+03	1.94E+09	

Abbreviations: Standard deviation (stdev).
* Error propagation according to the standard deviation of our temperature estimates.

Table 5
Morphological flow parameters of the Rancho Seco lava flows.

Parameter	Unit	Flow 5	stdev	Flow 6	stdev
Flow width W	m	581.2	0.71	629.2	0.49
Channel width w*	m	231.4	2.08	164.9	0.27
Length L	m	3943.6	0.85	2553.4	0.20
Thickness H	m	22.7	1.24	38.77	2.28
Slope Θ	°	2.66	0.0009	1.26	0.0001
Volume**	m^3	5.19E+07	2.85E+06	6.23E+07	3.66E+06

Abbreviation: Standard deviation (stdev)
* Obtained only with 4 and 2 profiles for F5 and F6, respectively.
** Volume= L×W×H

which the emplacement duration was estimated by Chevrel et al. (2016a, 2016b) to have been at least 35 years. In contrast, Deardorff and Cashman (2012) reported a total duration of 255–275 days for the ~1600-year BP Collier Cone lava flow in Oregon (~0.17 km^3), which represents only 24% of the total lava volume of Rancho Seco. The Lonquimay 1988–1990 flow (~0.23 km^3) with a total emplacement duration of 330 days (Naranjo et al., 1992), represents only 32% of the total lava volume of Rancho Seco. Flow front velocities of Rancho Seco fall in the range reported for the Lonquimay 1988–1990 lavas. Considering the average emplacement rate of 7 m^3/s reported for Lonquimay (Naranjo et al., 1992), an emplacement time for Rancho Seco's lavas of 3 years can be extrapolated. It is worth mentioning that in the cases of Collier and Lonquimay, effusion rates did not exceed 50 and 80 m^3/s, respectively. Values in this order of magnitude might have characterized the emplacement of the most volumetric flows at the beginning of Rancho Seco's eruption. An additional fact worth considering is that effusion rates decreased over time in some of the andesitic eruptions witnessed directly (e.g., Naranjo et al., 1992; Larrea et al., 2017), an observation that was not considered in the present work. Furthermore, some flows have been observed to continue advancing after eruption cessation (e.g., the 2011–2012 Cordón Caulle Lava Flow, Chile; Tuffen et al., 2013; Magnall et al., 2017; and the 2014 Sinabung lava flow, Indonesia; Carr et al., 2019).

6. Archaeological aspects and future volcanic hazards

The Michoacán lake basins enabled early human settlement because they offered favourable aquatic and riparian conditions with abundant resources (fish, birds, amphibians, etc.), which promoted the development of agriculture in the region. The latter was of great relevance for the development of the Tarascan Empire, which flourished from ~AD 1250 until the conquest by the Spaniards in AD 1530 (Pollard, 2008; Carot, 2013). In Michoacán, several urban archaeological sites have been discovered on young andesite lava flows (*malpaíses*) including Rancho Seco, where the ancient pre-Hispanic city of Angamuco was built (Fisher and Leisz, 2013; Fisher et al., 2017). This site exemplifies how an apparently inhospitable terrain was ingeniously modified to establish a city, with patterns that are similar to those observed at several other archaeological sites on lava flows in Michoacán (e.g. El Palacio and Malpaís Prieto near Zacapu; Forest et al., 2018, 2019). Although the exact benefits for choosing such seemingly unattractive rocky substrates as major building grounds remain enigmatic, one reason certainly resides in the fact that they provide large in situ quarries for construction materials utilized in diverse architectural elements (commoner and elite residences, altars, temples, walls, roads, etc.). By constructing their cities on top of the lava flows that served as a source of most of the heavy building materials, a substantial amount of energy (work hours) could be saved by avoiding long transportation distances (Ramírez-Uribe et al., 2019).

Historically, significant disasters have been associated with effusive volcanic activity from monogenetic volcanoes. One of the best-known examples in Mexico is Xitle volcano (Siebe, 2000), whose lavas buried the ancient towns of Cuicuilco and Copilco (important

Table 6
Summary of effusion rates, velocities, viscosities, and emplacement times of the Rancho Seco lava flows calculated using morphology-based methods.

	Viscosity [Pa·s]	Effusion rate [m^3/s]	% error*	Mass effusion rate^{QM} [kg/s]	Velocity [m/day]	% error	Time [days]	% error	Method
Flow 5	1.1E+09$^{\eta a}$	2^{Qu}	13	6.2E+03	16^{uJ}	13	250^{tV}	14	Jeffreys equation
	3.1E+05$^{\eta L}$	6^{Qw}	3	1.5E+04	39^{uQ}	6	101^{tV}	14	Kerr et al. (2006)
		5^{QV}	19	1.4E+04	36^{uL}	14	110^{tC}	14	Castruccio et al. (2013)
		13^{QGz}	5	3.3E+04	84^{uQ}	8	47^{tV}	8	Grätz-number
		19^{QV}	5	4.8E+04	123^{uQ}	8	32^{tKL}	11	Kilburn and Lopes (1991)
Flow 6	1.3E+09$^{\eta a}$	5^{Qu}	14	1.4E+04	19^{uJ}	14	137^{tV}	15	Jeffreys equation
	2.9E+05$^{\eta L}$	2^{Qw}	2	4.0E+03	6^{uQ}	6	464^{tV}	3	Kerr et al. (2006)
		3^{QV}	17	8.8E+03	12^{uL}	13	211^{tC}	13	Castruccio et al. (2013)
		5^{QGz}	6	1.3E+04	19^{uQ}	8	138^{tV}	8	Grätz-number
		10^{QV}	6	2.5E+04	34^{uQ}	8	75^{tKL}	12	Kilburn and Lopes (1991)
Mean F5-F6	1.2E+09	4		9.8E+03	18		194		Jeffreys equation
	3.0E+05	4		9.6E+03	23		283		Kerr et al. (2006)
		4		1.1E+04	24		161		Castruccio et al. (2013)
		9		2.3E+04	52		93		Grätz-number
		15		3.6E+04	79		54		Kilburn and Lopes (1991)

ηa Apparent viscosity of petrological approach. Maximum viscosity in *syn*-eruptive conditions.
ηL Liquid viscosity with Giordano et al. (2008). Minimum viscosity in syn-eruptive conditions.
Qu Estimated with $Q = uWH$. Eq. (11) of Appendix 3.
Qw Estimated with Eq. (14) of Appendix 3 using liquid viscosity. Yield strength in a growing crust regime of Kerr et al. (2006) with σ_c=2E+06 Pa best fit of Kerr and Lyman, (2007).
QGz Estimated with the Grätz number method. Eq. (19) of Appendix 3.
QV Estimated with *Effusion rate=Volume/Time*.
QM Estimated with *Mass effusion rate=Effusion rate*density*.
uJ Estimated with Jeffreys Eq. (9) of Appendix 3 using apparent viscosity of petrological approach.
uQ Estimated with $u = Q/WH$, re-organised Eq. (11) of Appendix 3.
uL Estimated with *Velocity=Length/Time*.
tV Estimated with *Time=Volume/Effusion rate*.
tC Estimated with Eq. (16) of Appendix 3. Yield strength in a growing crust regime of Castruccio et al. (2013) with σ_c=3E+05 Pa (best fit of Castruccio and Contreras, (2016).
tKL Estimated with Eq. (18) of Appendix 3. Emplacement time of Kilburn and Lopes (1991).
* Error propagation calculated following Chevrel et al. (2013), Appendix A.2, see also Chevrel et al. (2016b) and Lefler, (2011).

Table 7
Viscosities and yield strengths of the Rancho Seco lava flows calculated by morphology-based methods.

	ηJeffreys$^{\eta J}$ [Pa·s]	% error*	ηHulme (channel)$^{\eta H}$ [Pa·s]	% error	Yield strength from Hulme's model$^{\tau ch}$ [Pa]	% error	Yield strength$^{\tau o}$ [Pa]	% error
Flow 5	4.8E+08^{uC}	19	3.8E+06^{QC}	16	1.9E+04	8	2.6E+04	9
	2.1E+08^{uGz}	15	1.6E+06^{QGz}	10				
	1.4E+08^{uKL}	15	1.1E+06^{QKL}	10				
Flow 6	2.0E+09^{uC}	19	1.5E+05^{QC}	18	5.6E+03	7	2.1E+04	9
	1.3E+09^{uGz}	16	9.7E+04^{QGz}	9				
	7.0E+08^{uKL}	16	5.3E+04^{QKL}	9				
Mean F5-F6	1.2E+09		2.0E+06		1.2E+04		2.4E+04	
	7.5E+08		8.7E+05					
	4.2E+08		5.9E+05					

ηJ Estimated with Jeffreys Eq. (19) of Appendix 3.
uC Value using velocity asociated to yield strength in a growing crust regime of Castruccio et al. (2013).
uGz Value using velocity asociated to Grätz number.
uKL Value using velocity asociated to Kilburn and Lopes (1991).
ηH Based on Hulme's theory with Eq. (22) of Appendix 3.
QC Value using effusion rate asociated to yield strength in a growing crust regime of Castruccio et al. (2013).
QGz Value using effusion rate asociated to Grätz number.
QKL Value using effusion rate asociated to Kilburn and Lopes (1991).
τch Yield strength of a channelized lava with Eq. (21) of Appendix 3.
τo Yield strength at the base of a flow with Eq. (20) of Appendix 3.
* Error propagation calculated following Chevrel et al. (2013), Appendix A.2, see also Chevrel et al. (2016b) and Lefler, (2011).

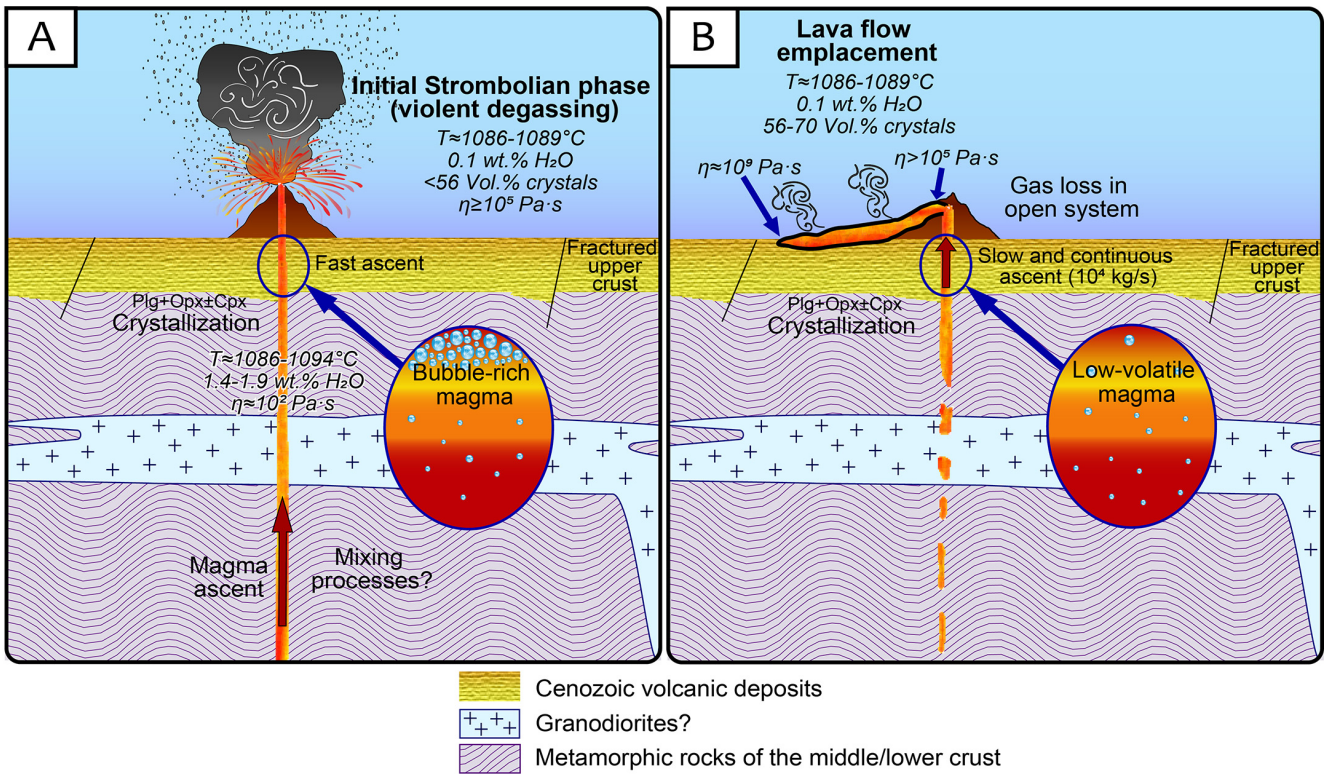

Fig. 13. Schematic model depicting magma ascent across the crust, crystallization, and subsequent eruption. A. Explosive phase of Rancho Seco volcano eruption characterized by violent-Strombolian activity with the ascent of large gas bubbles. B. Effusive phase of Rancho Seco volcano eruption characterized by efficient degassing of the magmatic system and a decrease in magma ascent rate. Stratigraphy based on Pasquaré et al. (1991).

Pre-Classic sites in the Mexico City Basin), and caused a great exodus that generated a population and economic imbalance that favoured the consolidation of Teotihuacan as the main center of power in the Mexico Basin (Vela, 2009). More recently, Jorullo volcano erupted in AD 1759, and its lava flows destroyed a sugar plantation in the Balsas basin of Michoacán (e.g. Gadow, 1930; Guilbaud et al., 2009; 2011). In the 20th century, also in Michoacán, the Paricutin volcano (1943–1952) generated great social problems because its lava completely buried the rural towns of Paricutin and San Juan Parangaricutiro (Flores-Covarrubias, 1945; Luhr and Simkin, 1993), fortunately without human fatalities. Human exodus led to the creation of the entirely new towns of Caltzontzin and Nuevo San Juan

Parangaricutiro. An eruption with the characteristics of the Rancho Seco volcano could have similar effects on the environment and society. Hence, the results obtained in this work together with our knowledge of other monogenetic eruptions in Mexico could be helpful to define future scenarios of volcanic hazards associated to lava flow emplacement in the MGVF.

7. Conclusions

This study provides new data for better understanding the effusive aspects of monogenetic volcanism in the MGVF. Andesite lava flows emitted from Rancho Seco volcano are relatively homogeneous in composition, indicating that probably one single batch of magma was gradually extruded. The lavas are the evolved products from a basaltic melt originally derived from the partial melting of the mantle wedge metasomatized by aqueous fluids from the subducting plate. Its subsequent evolution during ascent through the crust was dominated by fractional crystallization and minor assimilation of plutonic rocks of granodioritic composition.

Magma viscosities at pre-eruptive conditions were estimated to have been in the order of 10^2 Pa·s while lava viscosities (*syn*-eruptive) ranged between 10^5 considering no crystallization and 10^9 Pa·s when crystals contents are considered. Using these results and the final dimensions of the lava flows, various models were used to estimate the effusion rates for two well-exposed lava flows (0.05–0.06 km^3). We obtained a range of values between 2 and 19 m^3/s and lava flow emplacement durations of 32 to 464 days. The successive emplacement duration of all seven flows at Rancho Seco volcano (0.72 km^3) probably took 2 to 6 years (using a mean effusion rate ranging from 4 to 15 m^3/s).

These results could help define future eruptive scenarios and estimate associated volcanic hazards for monogenetic eruptions that produce lava flows in the MGVF, a volcanically still active region. The viscosity of such flows is relatively high and hence their velocity is likely too slow to cause loss of human lives. Nevertheless, such flows could seriously affect the infrastructure of entire towns and the outlined eruption dynamics should be considered useful for future volcanic risk management. The present study might also be of interest to archaeologists wishing to better understand the nature and origin of the rocky substrate of Rancho Seco's lava flows on which the enigmatic pre-Hispanic city of Angamuco was erected.

Declaration of Competing Interest

The authors declare that they have no known competing financial interests or personal relationships that could have appeared to influence the work reported in this paper.

Acknowledgments

Field and laboratory costs were defrayed by project DGAPA-UNAM-IN103618 (Dirección General de Asuntos del Personal Académico, UNAM) and DGAPA-UNAM-IN104221 granted to C. Siebe. Israel Ramírez benefitted from a CONACYT graduate-student fellowship (2017-2019), while Oryaelle Chevrel's work in Mexico was financed by a DGAPA-UNAM postdoctoral fellowship. We thank Noemí Salazar and Giovanni Sosa for help with the electron-microprobe at Instituto de Geofísica, Unidad Michoacán, UNAM. The LiDAR image was acquired as part of the "Legacies of Resilience, Lake Pátzcuaro Basin" (LORE-LPB) archaeological project granted to Christopher Fisher. Américo González-Esparza, Adriana Briseño, and Ernesto Andrade at UNAM Campus Morelia provided lodging facilities at the Mexican Array Radio Telescope (MEXART) near Coeneo during field campaigns. Capitán Fernando Valencia is thanked for skillful and safe flights over the study area. Journal editor Kelly Russel and an anonymous reviewer are both thanked for making valuable suggestions that were helpful to improve the original manuscript.

Appendices. Supplementary material

Supplementary data to this article can be found online at https://doi.org/10.1016/j.jvolgeores.2020.107169.

References

Agustín-Flores, J., Siebe, C., Guilbaud, M.N., 2011. Geology and geochemistry of Pelagatos, Cerro del Agua, and Dos Cerros monogenetic volcanoes in the Sierra Chichinautzin volcanic field, south of Mexico City. J. Volcanol. Geoth. Res. 201 (1–4), 143–162. https://doi.org/10.1016/j.jvolgeores.2010.08.010.

Beattie, P., 1993. Olivine-melt and orthopyroxene-melt equilibria. Contrib. Mineral. Petrol. 115, 103–111. https://doi.org/10.1007/BF00712982.

Blatter, D.L., Carmichael, I.S.E., 1998. Plagioclase-free andesites from Zitacuaro (Michoacan), Mexico: petrology and experimental constraints. Contrib. Mineral. Petrol. 132 (2), 121–138.

Blatter, D.L., Hammersley, L., 2010. Impact of the Orozco Fracture Zone on the central Mexican Volcanic Belt. J. Volcanol. Geoth. Res. 197, 67–84. https://doi.org/10.1016/j.jvolgeores.2009.08.002.

Caricchi, L., Burlini, L., Ulmer, P., Gerya, T., Vassalli, M., Papale, P., 2007. Non-Newtonian rheology of crystal-bearing magmas and implications for magma ascent dynamics. Earth Planet. Sci. Lett. 264, 402–419.

Carot, P., 2013. La larga historia purépecha. In: Aedo, A., Carot, P., Faba, P., Hernández, V., Hers, M.A. (Eds.), Miradas renovadas al Occidente indígena de México. Universidad Nacional Autónoma de México/Instituto Nacional de Antropología e Historia/Centro de Estudios Mexicanos y Centroamericanos, pp. 133–214.

Carr, B.B., Clarke, A.B., Vanderkluysen, L., Arrowsmith, J.R., 2019. Mechanisms of lava flow emplacement during an effusive eruption of Sinabung Volcano (Sumatra, Indonesia). J. Volcanol. Geotherm. Res. 382, 137–148. https://doi.org/10.1016/j.jvolgeores.2018.03.002.

Cashman, K.V., Soule, S.A., Mackey, B.H., Deligne, N.I., Deardorff, N.D., Dietterich, H.R., 2013. How lava flows: New insights from applications of lidar technologies to lava flow studies. Geosphere 9 (6), 1664–1680. https://doi.org/10.1130/GES00706.1.

Castruccio, A., Contreras, M.A., 2016. The influence of effusion rate and rheology on lava flow dynamics and morphology: a case study from the 1971 and 1988–1990 eruptions at Villarrica and Lonquimay volcanoes, Southern Andes of Chile. J. Volcanol. Geoth. Res. 327, 469–483. https://doi.org/10.1016/j.jvolgeores.2016.09.015.

Castruccio, A., Rust, A.C., Sparks, R.S.J., 2013. Evolution of crust- and core-dominated lava flows using scaling analysis. Bull. Volcanol. 75, 1–15. https://doi.org/10.1007/s00445-012-0681-2.

Cebriá, J.M., Martiny, B.M., López-Ruiz, J., Morán-Zenteno, D.J., 2011. The Paricutin calc-alkaline lavas: New geochemical and petrogenetic modelling constraints on the crustal assimilation process. J. Volcanol. Geoth. Res. 201, 113–125. https://doi.org/10.1016/j.jvolgeores.2010.11.011.

Chase, A.F., Chase, D.Z., Fisher, C.T., Leisz, S.J., Weishampel, J.F., 2012. Geospatial revolution and remote sensing LiDAR in Mesoamerican archaeology. Proc. Nat. Acad. Sci. 109 (32), 12916–12921.

Chevrel, M.O., Platz, T., Hauber, E., Baratoux, D., Lavallée, Y., Dingwell, D.B., 2013. Lava flow rheology: a comparison of morphological and petrological methods. Earth Planet. Sci. Lett. 384, 109–120. https://doi.org/10.1016/j.epsl.2013.09.022.

Chevrel, M.O., Siebe, C., Guilbaud, M.N., Salinas, S., 2016a. The AD 1250 El Metate shield volcano (Michoacán): Mexico's most voluminous Holocene eruption and its significance for archaeology and hazards. The Holocene 26 (3), 471–488. https://doi.org/10.1177/0959683615609757.

Chevrel, M.O., Guilbaud, M.N., Siebe, C., 2016b. The AD 1250 effusive eruption of El Metate shield volcano (Michoacán, Mexico): Magma source, crustal storage, eruptive dynamics, and lava rheology. Bull. Volcanol. 78 (4), 1–32. https://doi.org/10.1007/s00445-016-1020-9.

Chevrel, M.O., Pinkerton, H., Harris, A.J.L., 2019. Measuring the viscosity of lava in the field: a review. Earth Sci. Rev. 196, 1–13. https://doi.org/10.1016/j.earscirev.2019.04.024.

Cimarelli, C., Costa, A., Mueller, S., Mader, H.M., 2011. Rheology of magmas with bimodal crystal size and shape distributions: Insights from analog experiments. Geochem. Geophys. Geosyst. 12, 1–14. https://doi.org/10.1029/2011GC003606.

Corona-Chávez, P., Reyes-Salas, M., Garduño-Monroy, V.H., Israde-Alcántara, I., Lozano-Santa Cruz, R., Morton-Bermea, O., Hernández-Álvarez, E., 2006. Asimilación de xenolitos graníticos en el Campo Volcánico Michoacán-Guanajuato, el caso de Arócutin Michoacán. México. Rev. Mex. Cienc. Geol. 23 (2), 233–245.

Costa, A., Caricchi, L., Bagdassarov, N., 2009. A model for the rheology of particle-bearing suspensions and partially molten rocks. Geochem. Geophys. Geosyst. 10, 1525–2027.

Couch, S., Harford, C.L., Sparks, R.S.J., Carroll, M.R., 2003. Experimental constraints on the conditions of formation of highly calcic plagioclase microlites at the Soufrière Hills volcano. Montserrat. J. Petrol. 44, 1455–1475. https://doi.org/10.1093/petrology/44.8.1455.

Crabtree, S.M., Lange, R.A., 2011. Complex phenocryst textures and zoning patterns in andesites and dacites: evidence of degassing-induced rapid crystallization? J. Petrol. 52 (1), 3–38. https://doi.org/10.1093/petrology/egq067.

Crisp, J., Cashman, K.V., Bonini, J.A., Hougen, S.B., Pieri, D.C., 1994. Crystallization history of the 1984 Mauna Loa lava flow. J. Geophys. Res. 99, 7177–7198. https://doi.org/10.1029/93JB02973.

Deardorff, N.D., Cashman, K.V., 2012. Emplacement conditions of the c. 1,600-year bp Collier Cone lava flow, Oregon: a LiDAR investigation. Bull. Volcanol. 74 (9), 2051–2066. https://doi.org/10.1007/s00445-012-0650-9.

Deligne, N.I., Conrey, R.M., Cashman, K.V., Champion, D.E., Amidon, W.H., 2016. Holocene volcanism of the upper McKenzie River catchment, Central Oregon Cascades, USA. Geol. Soc. Am. Bull. 128 (11−12), 1618–1635. https://doi.org/10.1130/B31405.1.

Demant, A., 1978. Características del Eje Neovolcánico Transmexicano y sus problemas de interpretación. Rev. Mex. Cienc. Geol. 2 (2), 172–187.

Dietterich, H.R., Cashman, K.V., 2014. Channel networks within lava flows: Formation, evolution, and implications for flow behavior. J. Geophys. Res. Earth Surf. 119, 1704–1724. https://doi.org/10.1002/2014JF003103.

Dietterich, H.R., Downs, D.T., Stelten, M.E., Zahran, H., 2018. Reconstructing lava flow emplacement histories with rheological and morphological analyses: the Harrat Rahat volcanic field, Kingdom of Saudi Arabia. Bull. Volcanol. 80 (12), 1–23. https://doi.org/10.1007/s00445-018-1259-4.

Farquharson, J.I., James, M.R., Tuffen, H., 2015. Examining rhyolite lava flow dynamics through photo-based 3D reconstructions of the 2011–2012 lava flow field at Cordón-Caulle, Chile. J. Volcanol. Geother. Res. 304, 336–348. https://doi.org/10.1016/j.jvolgeores.2015.09.004.

Ferrari, L., Orozco-Esquivel, M.T., Manea, V., Manea, M., 2012. The dynamic history of the Trans-Mexican Volcanic Belt and the Mexico subduction zone. Tectonophys 522/523, 122–149. https://doi.org/10.1016/j.tecto.2011.09.018.

Fink, J., 1980. Surface folding and viscosity of rhyolite flows. Geology 8, 250–254. https://doi.org/10.1130/0091-7613(1980)8<250:SFAVOR>2.0.CO;2.

Fisher, C.T., Leisz, S.J., 2013. New perspectives on Purépecha urbanism through the use of LiDAR at the site of Angamuco. In: Comer, D.C., Harrower, M.J. (Eds.), Mapping Archaeological Landscapes from Space. Springer Briefs in Archaeology, pp. 199–210.

Fisher, C.T., Cohen, A.S., Fernández-Diaz, J.C., Leisz, S.J., 2017. The application of airborne mapping LiDAR for the documentation of ancient cities and regions in tropical regions. Quat. Int. 448, 129–138. https://doi.org/10.1016/j.quaint.2016.08.050.

Flores-Covarrubias, L., 1945. Cálculos para la determinación de la altura del cono del volcán del Parícutin. El Paricutín, México, D.F., UNAM, pp. 19–20.

Forest, M., Costa, L., Pereira, G., 2018. Le collectif face au big data: interprétation partagée et retro-validation des données LiDAR du site d'El Infiernillo, Michoacán, Mexique. Archéologies numériques. Openscience 1 (2), 1–15. https://doi.org/10.21494/ISTE.OP.2018.0298.

Forest, M., Costa, L., Combey, A., Dorison, A., Pereira, G., 2019. Testing Web Mapping and active Learning to Approach Lidar Data. Adv. Archaeol. Pract. 8 (1), 25–39.

Gadow, H., 1930. Jorullo. The history of the volcano of Jorullo and the reclamation of the devastated district by animals and plants. Cambridge University Press (100 p).

Gill, J.B., 1981. Orogenic Andesites and Plate Tectonics. Springer-Verlag, Berlin, Heidelberg, and New York (390 pp).

Giordano, D., Russell, J.K., Dingwell, D.B., 2008. Viscosity of magmatic liquids: a model. Earth Planet. Sci. Lett. 271, 123–134. https://doi.org/10.1016/j.epsl.2008.03.038.

Gómez-Tuena, A., Orozco-Esquivel, M.T., Ferrari, L., 2005. Petrogénesis ígnea de la Faja Volcánica Transmexicana. Bol. Soc. Geol. Mex. 57 (3), 227–283.

Gómez-Tuena, A., Mori, L., Straub, S.M., 2018. Geochemical and petrological insights into the tectonic origin of the Transmexican Volcanic Belt. Earth Sci. Rev. 183, 153–181. https://doi.org/10.1016/j.earscirev.2016.12.006.

Gómez-Vasconcelos, M.G., Garduño-Monroy, V.H., Macías, J.L., Layer, P.W., Benowitz, J.A., 2015. The Sierra de Mil Cumbres, Michoacán, México: Transitional volcanism between the Sierra Madre Occidental and the Trans-Mexican Volcanic Belt. J. Volcanol. Geoth. Res. 301, 128–147.

Griffiths, R.W., 2000. The dynamics of lava flows. Ann. Rev. Fluid Mechanics 32, 477–518. https://doi.org/10.1146/annurev.fluid.32.1.477.

Griffiths, R.W., Fink, J.H., 1993. Effects of surface cooling on the spreading of lava flows and domes. J. Fluid Mechanics 252. https://doi.org/10.1017/S0022112093003933 661–102.

Guilbaud, M.N., Siebe, C., Layer, P., Salinas, S., Castro-Govea, R., Garduño-Monroy, V.H., Le Corvec, N., 2011. Geology, geochronology, and tectonic setting of the Jorullo Volcano region, Michoacán, México. J. Volcanol. Geoth. Res. 201, 97–112. https://doi.org/10.1016/j.jvolgeores.2010.09.005.

Guilbaud, M.N., Siebe, C., Layer, P., Salinas, S., 2012. Reconstruction of the volcanic history of the Tacámbaro-Puruarán area (Michoacán, México) reveals high frequency of Holocene monogenetic eruptions. Bull. Volcanol. 74 (5), 1187–1211. https://doi.org/10.1007/s00445-012-0594-0.

Guilbaud, M.N., Siebe, C., Salinas, S., 2009. Excursions to Paricutin and Jorullo (Michoacán), the youngest volcanoes of the Trans-Mexican Volcanic Belt. A commemorative fieldtrip on the occasion of the 250th anniversary of Volcán Jorullo's birthday on September 29, 1759. Impretei S.A., México, D.F.

Guilbaud, M.N., Siebe, C., Widom, E., Rasoazanamparany, C., Salinas, S., Castro-Govea, R., 2019. Petrographic, geochemical, and isotopic (Sr-Nd-Pb-Os) study of Plio-Quaternary volcanics and the Tertiary basement in the Jorullo-Tacámbaro area, Michoacán-Guanajuato Volcanic Field. México. J. Petrol. 60 (12), 2317–2338. https://doi.org/10.1093/petrology/egaa006.

Harris, A.J.L., Rowland, S.K., 2015. Lava flows and rheology. In: Sigurdsson, et al. (Eds.), The Encyclopedia of Volcanoes. Academic Press, pp. 321–342 https://doi.org/10.1016/B978-0-12-385938-9.00017-1.

Hasenaka, T., 1994. Size, distribution, and magma output rate for shield volcanoes of the Michoacán-Guanajuato volcanic field, Central Mexico. J. Volcanol. Geoth. Res. 63, 13–31. https://doi.org/10.1016/0377-0273(94)90016-7.

Hasenaka, T., Carmichael, I.S.E., 1985. The cinder cones of Michoacán-Guanajuato, Central Mexico: their age, volume and distribution, and magma discharge rate. J. Volcanol. Geoth. Res. 25, 104–124. https://doi.org/10.1016/0377-0273(85)90007-1.

Hawkesworth, C.J., O'nions, R.K., Pankhurst, R.J., Hamilton, P.J., Evensen, N.M., 1977. A geochemical study of island-arc and back-arc tholeiites from the Scotia Sea. Earth Planet. Sci. Lett. 36 (2), 253–262. https://doi.org/10.1130/0016-7606(1999)111<1550:MBEIAL>2.3.CO;2.

Hulme, G., 1974. The interpretation of lava flow morphology. Geophys. Jour. Roy. Astronom. Soc. 39, 361–383. https://doi.org/10.1111/j.1365-246X.1974.tb05460.x.

Hulme, G., Fielder, G., 1977. Effusion rates and rheology of lunar lavas. Phil. Trans. Roy. Soc. A 285, 227–234.

Hunt, J.A., Pyle, D.M., Mather, T.A., 2019. The geomorphology, structure, and lava flow dynamics of peralkaline rift volcanoes from high-resolution digital elevation models. Geochem. Geophys. Geosyst. 20 (3), 1508–1538. https://doi.org/10.1029/2018GC008085.

INEGI, 2019. Instituto Nacional de Estadística, Geografía e Informática. "Modelos Digitales de Elevación (MDE) -Descripción". https://www.inegi.org.mx/contenidos/temas/mapas/relieve/continental/metadatos/mde.pdf (accessed 20 December 2019).

Inomata, T., Triadan, D., Vázquez, V.A., Fernández-Díaz, J.C., Omori, T., Méndez, M.B., García, M., Beach, T., Cagnato, C., Aoyama, K., Nasu, H., 2020. Monumental architecture at Aguada Fénix and the rise of Maya civilization. Nature (June 2020), 1–4 https://doi.org/10.1038/s41586-020-2343-4.

Irvine, T.N., Baragar, W.R.A., 1971. A guide to the chemical classification of the common volcanic rocks. Can. Jour. Earth Sci. 8, 523–548.

Jeffreys, H., 1925. The flow of water in an inclined channel of rectangular section. The London, Edinburgh, and Dublin Philosophical Magazine and Journal of Science 49 (293), 793–807. https://doi.org/10.1080/14786442508634662.

Kerr, R.C., Lyman, A.W., 2007. Importance of surface crust strength during the flow of the 1988–1990 andesite lava of Lonquimay Volcano, Chile. J. Geophys. Res. 112, 1–8. https://doi.org/10.1029/2006JB004522.

Kerr, R.C., Griffiths, R.W., Cashman, K.V., 2006. Formation of channelized lava flows on an unconfined slope. J. Geophys. Res. 111, 1–13. https://doi.org/10.1029/2005JB004225.

Kilburn, C.R.J., Lopes, R., 1991. General patterns of flow field growth: Aa and blocky lavas. J. Geophys. Res. 96 (B12), 19721–19732. https://doi.org/10.1029/91JB01924.

Kolzenburg, S., Giordano, D., Thordarson, T., Höskuldsson, A., Dingwell, D.B., 2017. The rheological evolution of the 2014/2015 eruption at Holuhraun, Central Iceland. Bull. Volcanol. 79, 1–16. https://doi.org/10.1007/s00445-017-1128-6.

Krauskopf, K., 1948. Mechanism of eruption at Paricutin volcano, Mexico. Geol. Soc. Am. Bull. 59, 711–731. https://doi.org/10.1130/0016-7606(1948)59[1267:LMAPVM]2.0.CO;2.

Kshirsagar, P., Siebe, C., Guilbaud, M.N., Salinas, S., 2015. Late Pleistocene Alberca de Guadalupe maar volcano (Zacapu basin, Michoacán): Stratigraphy, tectonic setting, and paleo-hydrogeological environment. J. Volcanol. Geoth. Res. 304, 214–236. https://doi.org/10.1016/j.jvolgeores.2015.09.003.

Kshirsagar, P., Siebe, C., Guilbaud, M., Salinas, S., 2016. Geological and environmental controls on the change of eruptive style (phreatomagmatic to Strombolian-effusive) of Late Pleistocene El Caracol tuff cone and its comparison with adjacent volcanoes around the Zacapu basin (Michoacán, México). J. Volcanol. Geotherm. Res. 318, 114–133. https://doi.org/10.1016/j.jvolgeores.2016.03.015.

Larrea, P., Salinas, S., Widom, E., Siebe, C., Abbitt, R.J.F., 2017. Compositional and volumetric development of a monogenetic lava flow field: the historical case of Paricutin (Michoacán, Mexico). J. Volcanol. Geoth. Res. 348, 36–48. https://doi.org/10.1016/j.jvolgeores.2017.10.016.

Larrea, P., Widom, E., Siebe, C., Salinas, S., Kuentz, D., 2019. A re-interpretation of the petrogenesis of Paricutin volcano: Distinguishing crustal contamination from mantle heterogeneity. Chem. Geol. 504, 66–82. https://doi.org/10.1016/j.chemgeo.2018.10.026.

Lavallée, Y., Hess, K.U., Cordonnier, B., Dingwell, D.B., 2007. Non-Newtonian rheological law for highly crystalline dome lavas. Geology 35, 843–846.

Le Bas, M.J., Le Maitre, R.W., Streckeisen, A., Zanettin, B., 1986. A chemical classification of volcanic rocks based on the total alkali–silica diagram. J. Petrol. 27, 745–750.

Lefler, E., 2011. Genauigkeitsbetrachtung bei der Ermittlung rheologischer Parameter von Lavaströmen aus Fernerkundungsdaten. Alemania. Freie Universität Berlin. Diplomarbeit, Berlín (68 pp).

Lejeune, A.M., Richet, P., 1995. Rheology of crystal-bearing silicate melts: an experimental study at high viscosities. J. Geophys. Res. 100 (B3), 4215–4229. https://doi.org/10.1029/94JB02985.

Luhr, J.F., Carmichael, I.S.E., 1985. Jorullo volcano, Michoacán, Mexico (1759–1774): the earliest stages of fractionation in calc-alkaline magmas. Contrib. Mineral. Petrol. 90 (2–3), 142–161. https://doi.org/10.1007/BF00378256.

Luhr, J.F., Simkin, T., 1993. Paricutin: The Volcano Born in a Mexican Cornfield. Geoscience Press (427 pp).

Magnall, N., James, M.R., Tuffen, H., Vye-Brown, C., 2017. Emplacing a cooling-limited rhyolite lava flow: Similarities with basaltic lava flows. Frontiers Earth Sci. 5, 1–19. https://doi.org/10.3389/feart.2017.00044.

Magnall, N., James, M.R., Tuffen, H., Vye-Brown, C., Schipper, C.I., Castro, J.M., Davies, A.G., 2019. The origin and evolution of breakouts in a cooling-limited rhyolite lava flow. Geol. Soc. Am. Bull. 131 (1–2), 137–154. https://doi.org/10.1130/B31931.1.

McAnany, P.A., 2020. Large-scale early Maya sites revealed by lidar. Nature, 1–2 https://doi.org/10.1038/d41586-020-01570-8.

McDonough, W.F., Sun, S.S., 1995. The composition of the Earth. Chem. Geol. 120, 223–253.

Naranjo, J.A., Sparks, R.S.J., Stasiuk, M.V., Moreno, H., Ablay, G.J., 1992. Morphological, structural and textural variations in the 1988–1990 andesite lava of Lonquimay Volcano, Chile. Geol. Mag. 12 (6), 657–678. https://doi.org/10.1017/S0016756800008426.

Nguyen, C.T., Gonnermann, H.M., Houghton, B.F., 2014. Explosive to effusive transition during the largest volcanic eruption of the 20th century (Novarupta 1912, Alaska). Geology 42 (8), 703–706. https://doi.org/10.1130/G35593.1.

Nichols, R.L., 1939. Viscosity of lava. J. Geol. 47, 290–302.

Nixon, G.T., 1982. The relationship between Quaternary volcanism in Central Mexico and the seismicity and structure of subducted ocean lithosphere. Geol. Soc. Am. Bull. 93 (6), 514–523.

Osorio-Ocampo, S., Macías, J.L., Pola, A., Cardona-Melchor, S., Sosa-Ceballos, G., Garduño-Monroy, V.H., Layer, P.W., García-Sánchez, L., Perton, M., Benowitz, J., 2018. The eruptive history of the Pátzcuaro Lake area in the Michoacán Guanajuato Volcanic Field, Central México: Field mapping, C-14 and $^{40}Ar/^{39}Ar$ geochronology. J. Volcanol. Geoth. Res. 358, 307–328. https://doi.org/10.1016/j.jvolgeores.2018.06.003.

Ownby, S., Delgado-Granados, H., Lange, R.A., Hall, C., 2007. Volcán Tancítaro, Michoacán, Mexico, 40Ar/39Ar constraints on its history of sector collapse. J. Volcanol. Geoth. Res. 161, 1–14. https://doi.org/10.1016/j.jvolgeores.2006.10.009.

Pardo, M., Suárez, G., 1995. Shape of the subducted Rivera and Cocos plates in southern Mexico: Seismic and tectonic implications. J. Geophys. Res. 100 (B7), 12357–12373. https://doi.org/10.1029/95JB00919.

Pasquaré, G., Ferrari, L., Garduño, V., Tibaldi, A., Vezzoli, L., 1991. Geology of the central sector of the Mexican Volcanic Belt, States of Guanajuato and Michoacan. Geol. Soc. Am., Map and Chart Series MCH072 (20 p).

Pérez-Orozco, J.D., Sosa-Ceballos, G., Garduño-Monroy, V.H., Avellán, D.R., 2018. Felsic-intermediate magmatism and brittle deformation in Sierra del Tzirate (Michoacán Guanajuato Volcanic Field). J. S. Am. Earth Sci. 85, 81–96. https://doi.org/10.1016/j.jsames.2018.04.021.

Pinkerton, H., 1987. Factor affecting the morphology of lava flows. Endeavour 11 (2), 73–79. https://doi.org/10.1016/0160-9327(87)90241-9.

Pinkerton, H., Sparks, R.S.J., 1976. The 1975 sub-terminal lavas, Mount Etna: a case history of the formation of a compound lava field. J. Volcanol. Geoth. Res. 1, 167–182.

Pinkerton, H., Wilson, L., 1994. Factor controlling the lengths of channel-fed lava flows. Bull. Volcanol. 6, 108–120.

Pioli, L., Erlund, E., Johnson, E., Cashman, K., Wallace, P., Rosi, M., Delgado-Granados, H., 2008. Explosive dynamics of violent Strombolian eruptions: the eruption of Parícutin Volcano 1943–1952 (Mexico). Earth Planet. Sci. Lett. 271 (1–4), 359–368. https://doi.org/10.1016/j.epsl.2008.04.026.

Pioli, L., Azzopardi, B.J., Cashman, K.V., 2009. Controls on the explosivity of scoria cone eruptions: Magma segregation at conduit junctions. J. Volcanol. Geoth. Res. 186 (3–4), 407–415. https://doi.org/10.1016/j.jvolgeores.2009.07.014.

Pollard, H.P., 2008. A model of the emergence of the Tarascan state. Anc. Mesoam. 19, 217–230.

Putirka, K., 2005. Igneous thermometers and barometers based on plagioclase + liquid equilibria: tests of some existing models and new calibrations. Am. Mineral. 90, 336–346. https://doi.org/10.2138/am.2005.1449.

Ramírez-Uribe, I., Siebe, C., Salinas, S., Guilbaud, M.N., Layer, P., Benowitz, J., 2019. ^{14}C and $^{40}Ar/^{39}Ar$ radiometric dating and geologic setting of young lavas of Rancho Seco and Mazcuta volcanoes hosting archaeological sites at the margins of the Pátzcuaro and Zacapu lake basins (Central Michoacán, Mexico). J. Volcanol. Geoth. Res. 388, 1–22. https://doi.org/10.1016/j.jvolgeores.2019.106674.

Rasoazanamparany, C., Widom, E., Siebe, C., Guilbaud, M.N., Spicuzza, M.J., Valley, J.W., Valdez, G., Salinas, S., 2016. Temporal and compositional evolution of Jorullo volcano, Mexico: Implications for magmatic processes associated with a monogenetic eruption. Chem. Geol. 434, 62–80. https://doi.org/10.1016/j.chemgeo.2016.04.004.

Reyes-Guzmán, N., Siebe, C., Chevrel, M.O., Guilbaud, M.N., Salinas, S., Layer, P., 2018. Geology and radiometric dating of Quaternary monogenetic volcanism in the western Zacapu lacustrine basin (Michoacán, México): implications for archeology and future hazard evaluations. Bull. Volcanol. 80 (2), 1–18. https://doi.org/10.1007/s00445-018-1193-5.

Siebe, C., 2000. Age and archaeological implications of Xitle volcano, southwestern basin of Mexico-City. J. Volcanol. Geoth. Res. 104 (1–4), 45–64. https://doi.org/10.1016/S0377-0273(00)00199-2.

Siebe, C., Macías, J.L., 2006. Volcanic hazards in the Mexico City metropolitan area from eruptions at Popocatépetl, Nevado de Toluca, and Jocotitlán stratovolcanoes and monogenetic scoria cones in the Sierra Chichinautzin Volcanic Field. In: Siebe, C., Macías, J.L., Aguirre, G. (Eds.), Neogene-Quaternary Continental Margin Volcanism: A Perspective from Mexico. Geol. Soc. Amer. Spec. Pap.. 402, pp. 253–329

Siebe, C., Rodríguez-Lara, V., Schaaf, P., Abrams, M., 2004. Geochemistry, Sr-Nd isotope composition, and tectonic setting of Holocene Pelado, Guespalapa, and Chichinautzin scoria cones, south of Mexico-City. J. Volcanol. Geoth. Res. 130 (3–4), 197–226. https://doi.org/10.1016/S0377-0273(03)00289-0.

Siebe, C., Guilbaud, M.N., Salinas, S., Kshirsagar, P., Chevrel, M.O., De la Fuente, J.R., Hernández-Jiménez, A., Godínez, L., 2014. Monogenetic volcanism of the Michoacán-Guanajuato Volcanic Field: Maar craters of the Zacapu basin and domes, shields, and scoria cones of the Tarascan highlands (Paracho-Paricutin region). Field Guide, Pre-meeting Fieldtrip (Nov. 13-17) for the 5th International Maar Conference (5IMC-IAVCEI), Querétaro, México (33 pp).

Sun, S.S., McDonough, W.F., 1989. Chemical and isotopic systematics of oceanic basalts: Implications for mantle composition and processes. In: Saunders, A.D., Norry, M.J. (Eds.), Magmatism in the Ocean Basins. Geol. Soc. Lon. Spec. Publ. 42, pp. 313–345.

Tenzer, R., Sirguey, P., Rattenbury, M., Nicolson, J., 2011. A digital rock density map of New Zealand. Comput. Geosci. 37 (8), 1181–1191. https://doi.org/10.1016/j.cageo.2010.07.010.

Tuffen, H., James, M.R., Castro, J.M., Schipper, C.I., 2013. Exceptional mobility of an advancing rhyolitic obsidian flow at Cordon Caulle volcano in Chile. Nat. Commun. 4, 1–7. https://doi.org/10.1038/ncomms3709.

Vela, E., 2009. Los volcanes de México. Arqueología Mexicana 16 (95), 1–88.

Verma, S.P., Hasenaka, T., 2004. Sr, Nd, and Pb isotopic and trace element geochemical constraints for a veined-mantle source of magmas in the Michoacan-Guanajuato volcanic field, west-central Mexican volcanic belt. Geochem. J. 38 (1), 43–65. https://doi.org/10.2343/geochemj.38.43.

Walker, G.P.L., 1973. Lengths of lava flows. Phil. Trans. Roy. Soc. London Series A 274 (1238), 107–118.

Waters, L.E., Lange, R.A., 2015. An updated calibration of the plagioclase-liquid hygrometer-thermometer applicable to basalts through rhyolites. Am. Mineral. 100, 2172–2184. https://doi.org/10.2138/am-2015-5232.

Wilcox, R.E., 1954. The petrology of Paricutin volcano. U.S. Geol. Surv. Bull. 965-C, 281–354.

Wilson, L., Head, J.W., 1994. Mars: Review and analysis of volcanic eruption theory and relationships to observed landforms. Rev. Geophys. 32, 221–263. https://doi.org/10.1029/94RG01113.

Younger, Z.P., Valentine, G.A., Gregg, T.K.P., 2019. A'ā lava emplacement and the significance of rafted pyroclastic material: Marcath volcano (Nevada, USA). Bull. Volcanol. 81, 1–50. https://doi.org/10.1007/s00445-019-1309-6.